The contemporary force balance in a wide accretionary wedge: numerical models of the south-central Hikurangi margin of New Zealand

Susan Ellis[1], Francesca Ghisetti[2], Philip M. Barnes[3], Carolyn Boulton[4], Åke Fagereng[5], and Susanne Buiter[6]

[1] GNS Science, PO Box 30-368, Avalon, Lower Hutt 5010, New Zealand

[2] TerraGeoLogica, Ruby Bay, New Zealand

[3] National Institute of Water & Atmospheric Research, NIWA, Wellington

[4] School of Geography, Environment, and Earth Sciences, Victoria University of Wellington, Wellington, New Zealand

[5] Cardiff University, Park Place, Cardiff CF10 3AT, United Kingdom

[6] Geological Survey of Norway, Leiv Eirikssons vei 39, 7040 Trondheim, Norway

Email addresses:

s.ellis@gns.cri.nz

francesca.ghisetti@terrageologica.com

Philip.Barnes@niwa.co.nz

carolyn.boulton@vuw.ac.nz

FagerengA@cardiff.ac.uk

Susanne.Buiter@ngu.no

Paper submitted *in original form* March 18th 2019

Paper accepter July 9th 2019

Abbreviated title: **"The force balance in a wide accretionary wedge"**

Corresponding Author: Susan Ellis, s.ellis@gns.cri.nz

phone: +64 4 570 4730, fax +64 4 570 4600

Summary

The south-central Hikurangi subduction margin (North Island, New Zealand) has a wide, low-taper accretionary wedge that is frontally accreting a > 3 km-thick layer of sediments, with deformation currently focused near the toe of the wedge. We use a geological model based on a depth-converted seismic section, together with physically realistic parameters for fluid pressure, and sediment and décollement friction based on laboratory experiments, to investigate the present-day force balance in the wedge. Numerical models are used to establish the range of physical parameters compatible with the present-day wedge geometry and mechanics. Our analysis shows that the accretionary wedge stability and taper angle require either high to moderate fluid pressure on the plate interface, and/or weak frictional strength along the décollement. The décollement beneath the outer wedge requires a relatively weaker effective strength than beneath the inner (consolidated) wedge. Increasing density and cohesion with depth make it easier to attain a stable taper within the inner wedge, while anything that weakens the wedge- such as high fluid pressures and weak faults - make it harder. Our results allow a near-hydrostatic wedge fluid pressure, sub-lithostatic fluid overpressure at the subduction interface, and friction coefficients compatible with measurements from laboratory experiments on weak clay minerals.

Keywords

Subduction zone processes

Continental margins: convergent

High strain deformation zones

New Zealand

Rheology and friction of fault zones

Mechanics, theory, and modelling

1.

1. Introduction

The rate and style of accretion at convergent margins exerts a fundamental control on the mechanical strength and fluid state of sediments along and above the subduction plate boundary décollement (e.g., Moore et al. 1990; Casey Moore et al. 1998; von Huene and Klaeschen 1999; Kopp and Kukowski 2003; Moore et al. 2007). Conversely, the frictional properties, fluid state, and the geometry of stratigraphic units undergoing deformation within the décollement influence the long-term growth and morphology of an accretionary wedge because they control its basal strength, and hence the maximum permissible wedge taper angle (Dahlen 1990). The relationship between décollement properties and wedge geometry implies that the dynamics of accretionary wedges and the larger-scale subduction process are closely linked. Décollement strength and stability also control the occurrence and frequency of large megathrust earthquakes that severely affect human livelihood and infrastructure (e.g. Scholz 1998; Kodaira et al. 2004; den Hartog and Spiers 2013).

The first-order frictional strength of a wedge's basal décollement can be estimated using a static force balance approach via the analytical critical wedge theory (Davis et al. 1983; Dahlen 1990). Critical wedge calculations commonly assume constant values for the frictional strength and fluid overpressure state of the wedge and décollement, although modifications can be made to consider variations in fluid overpressure and/or density with depth (Skarbek and Rempel 2017). However, many accretionary systems are not fully described by assuming a critical wedge force balance, because they pass transiently through several non-critical states as the strength of upper plate faults and of the décollement vary laterally and evolve through time (see review in Buiter 2012). Understanding the transient

nature of wedge dynamics and its effect on present-day conditions is necessary to determine whether a subduction décollement is strong or weak, how stress is accumulated along it, and whether it will potentially slip in large earthquakes (Wang and Hu 2006). Analogue and numerical forward models have extended critical wedge theory and highlighted the strong impact of heterogeneous material properties that vary in space and time on the evolution of non-critical thrust wedges (eg, Colletta et al. 1991; Storti and McClay 1995; Koyi and Vendeville 2003; Smit et al. 2003; Schreurs et al. 2006; Yamada et al. 2006; Buiter 2012).

Here, we use numerical dynamic models to investigate heterogeneous wedge dynamics of an active convergent margin – the Hikurangi subduction zone of New Zealand. Despite an absence of megathrust earthquakes recorded historically on the Hikurangi subduction zone during New Zealand's short (ca. 150 years) historic earthquake record, the subduction fault is considered to pose a large seismic and tsunami hazard (Stirling et al. 2012; Power et al. 2016; Clark et al., 2019). In addition, the offshore Hikurangi accretionary wedge exhibits major along-strike variations in wedge morphology, with a steep narrow wedge (north Hikurangi) transitioning to an extremely wide, low-taper wedge (southern Hikurangi; Wallace et al., 2009; Fagereng 2011). This is mirrored by a change from shallow to deep interseismic coupling on the subduction interface (Wallace et al. 2004). Determining the mechanical cause of such along-strike variations is critical to future estimates of seismic risk of the Hikurangi margin, and to inform subduction studies globally.

We focus on the present-day force balance of the wide, offshore low-taper south-central Hikurangi accretionary wedge using a geological section interpreted from seismic reflection data (Fig. 1) (Ghisetti et al. 2016; Plaza-Faverola et al. 2016). We develop numerical models that replicate the present-day deformation (Barnes et al. 2010, 2018; Ghisetti et al. 2016), with the aim of constraining the admissible wedge and décollement friction strength and fluid pressure conditions. We show that, in comparison to the northern Hikurangi wedge, which is

unlikely to be in critical force balance, south-central Hikurangi can be at or near critical wedge equilibrium with moderate fluid pressures (even hydrostatic) in the wedge, provided there are moderate to high fluid overpressures along a weak basal décollement. Our results help to constrain the relative contributions of weak, clay-dominated rheology and fluid pressures along the décollement of a low-tapered critical accretionary wedge. We show that the present-day wedge force balance allows a strengthening in basal friction with increasing temperature and pressure. We also demonstrate the effect of weak upper plate faults on wedge stability.

2. Geological setting and previous work

The Hikurangi accretionary wedge formed in response to oblique subduction of oceanic Pacific lithosphere beneath the North Island of New Zealand since ca. 20 Ma (Ballance 1976; Lewis and Pettinga 1993) (Fig. 1). The subducting Pacific plate in this region is composed of the anomalously thick (>15 km) oceanic crust of the Cretaceous Hikurangi Plateau (Davy & Wood 1994; Mortimer & Parkinson 1996; Davy et al. 2008). After the onset of subduction, an imbricated thrust wedge of Cretaceous, Paleogene, and early Miocene sediments developed (Pettinga 1982), and was subsequently exposed onland by forearc uplift associated with subduction of the buoyant plateau crust. In the Neogene, deformation in the south and central Hikurangi subduction zone expanded eastward to form a broad (ca.130 km) low-taper (<4°) offshore accretionary wedge that incorporated late Cenozoic accreted trench-fill turbidites (Lewis and Pettinga 1993; Barnes et al. 2010). Present-day relative oblique convergence rates between the Pacific and Australian plates in our study area are ca. 43 mm/yr, increasing to ca. 48 mm/yr further north (DeMets et al. 1994; Beavan et al., 2002; Wallace et al., 2004; Fig. 1a), while owing to rotation of the Hikurangi forearc, trench-

perpendicular rates are ca. 35 mm/yr in the study area, increasing to 60 mm/yr in the north (Wallace et al. 2004; Fig. 1a).

Insert Fig. 1 here

In contrast to the northern Hikurangi wedge (north of Hawke Bay) which is relatively sediment-starved, narrow (60-70 km wide) and steeply-tapered (>10°), the wide (ca. 130-km) accretionary wedge in our study area has a taper angle of ≤ 4° and a thick trench sedimentary sequence (3-4 km thick) at the deformation front (Fig. 1; Lewis et al. 1998; Pedley et al. 2010; Barker et al. 2009, 2018). South-central Hikurangi wedge has a prominent protothrust zone extending along-strike for ca. 200 km (Barnes et al. 2010; 2018). The offshore frontal wedge in this region presently accommodates ca. 30-95% of the margin-normal convergence rate (Beavan et al. 2002; Ghisetti et al. 2016; Barnes et al. 2018).

The Hikurangi wedge morphology (Fig. 1a) has been used previously to infer time-averaged effective strength along the plate interface. Fagereng (2011) used the analytical formulation of critical wedge theory to compare the shallow and steep taper angles of southern and northern Hikurangi. He suggested that a very weak basal décollement accompanied by higher fluid overpressure causes the shallow taper in the south, while the steep taper in northern Hikurangi requires a higher décollement strength and/or lower fluid pressure. Skarbek and Rempel (2017) extended the critical wedge analysis to consider the effects of compaction on porosity and density. They also found that the low taper of the south-central margin required high décollement fluid pressure, whereas northern Hikurangi did not. Neither of these studies explicitly considered variations in wedge and basal strength with depth, the effect of upper plate thrust faults, and variations in geometry between the inner and outer wedge. To do so requires more detailed numerical models of specific wedge transects, something we address in the following sections for south-central Hikurangi.

2.1 South-Central Hikurangi wedge transect

Our study is based on the interpretation of a ca. 150 km long geological transect across the widest part of the accretionary wedge from just offshore of Cape Turnagain south-eastwards to Bennett Knoll Seamount (Fig. 1b). The transect, referred to as "Extended Transect 2" ("ET2"; Fig. 1b; Fig. 2), is developed from two joined depth seismic lines (05CM-38 and SO191-4) (cf. Barker et al. 2009; Ghisetti et al. 2016; Plaza-Faverola et al. 2016; Barnes et al. 2018). Uninterpreted images of the PSDM section 05CM-38 and depth-converted section SO191-4 at various scales are shown in Plaza-Faverola et al 2016, Ghisetti et al 2016, and Barnes et al 2018, and are therefore not repeated here. The geological transect is oriented ca. 112˚, i.e. slightly oblique to the direction of margin-normal convergence. For this paper we extended Transect 2 of Ghisetti et al. (2016) landward using the interpretation of line 05CM-38 from Plaza-Faverola et al. (2016) and the tie data from the exploration well Tawatawa-1 (Tap Oil Ltd, 2004; Fig. 1). Details of the transect are outlined in Supplementary file S1, and a summary is given below.

Along ET2, Pōrangahau Ridge approximately separates an "outer wedge" to the east from an "inner wedge" to the west (Fig. 2a). Within the "outer wedge" the geological interpretation is relatively more detailed, made possible by prominent and more continuous reflections from markers that separate units with contrasting seismic facies and velocity and are imbricated along thrust faults (these faults and units separated by reflectors R7 to R0 are shown on Fig. 2a; cf. Ghisetti et al. 2016). However, the ages of the inferred stratigraphic sequence are not well constrained. West of Pōrangahau Ridge (Fig. 2a) even the structure and stratigraphic architecture of the "inner wedge" is poorly constrained, because disruption and imbrication of the sequence by thrusting, combined with poor seismic resolution, makes interpretation of marker reflections and the décollement increasingly challenging with depth (Field et al. 1997; Barker et al. 2009; Barnes et al. 2010; Ghisetti et al., 2016; Plaza-Faverola et al. 2016). For

this reason, on Fig. 2a we distinguish only three units that broadly correlate with equivalent units in the outer wedge. Similarly, we have simplified the position of the inner wedge basal décollement. The simplest interpretation is that it is a continuous, gently-dipping feature beneath Pōrangahau Ridge, but in our study we also consider the effects of a possible step-down (Plaza-Faverola et al. 2016) as indicated on Fig. 2a. Thrust faults in the inner wedge west of Pōrangahau Ridge (Fig. 2a) can be identified by offset of markers at the shallowest levels (above R7) but their position in the deepest portion of the consolidated wedge is poorly defined. We have chosen to extrapolate them down into the décollement using a listric geometry that replicates the geometry in the outer wedge. More details about the wedge interpretation and stratigraphy can be found in Supplement 1.

Reconstructions of the past ca. 2 Ma of outer wedge deformation by Ghisetti et al. (2016) and further analysis of recent frontal deformation by Barnes et al. (2018) indicate that the major controls on wedge deformation can be attributed to distributed, pervasive shortening, the amount of displacement along individual faults and out-of-sequence reactivation, and detachment along the basal décollement. The control exerted by mechanical contrast between units is considered a second-order effect. For this reason, and since available data make it impossible to provide a detailed litho-stratigraphy of the inner wedge, our numerical models use one undifferentiated wedge unit above the basal décollement, as shown in Fig. 2b. Although the wedge composition is here approximated by using one material only, the effects of wedge consolidation on mechanical properties are explored in some of the models where cohesion and density increase with depth.

Insert Fig. 2 here

2.2 Deformation and present-day shortening rate within ET2

Our model experiments focus on brittle wedge deformation (i.e. they use a strain-rate-insensitive rheology), so that the exact rate of shortening used in the models will not affect the analysis of wedge stability and deformation style. Nevertheless, we attempt to constrain the total shortening rate (i.e., the net convergence rate between the incoming plate and the upper plate landward edge of ET2) to roughly match estimates from geological and geodetic studies.

An upper bound on the recent shortening rate for ET2 is given by the total plate-normal convergence rate, 31-40 mm/yr for the southern Hikurangi margin (Beavan et al. 2002; Wallace et al. 2004, 2012). While some of this is absorbed by deformation on-land, Nicol and Wallace (2007) estimate that the total component of offshore plate-normal convergence caused by under-thrusting of the lower plate and shortening of the accretionary wedge is ca. 3 cm yr^{-1}. However, the net shortening rate from ca. 0.1 Ma to Present estimated from macroscopic folding and faulting along transect T02 is only 1 cm/yr (Ghisetti et al. 2016), roughly in line with an earlier estimate by Barnes and Mercier de Lepinay (1997). The shortening rates derived from retro-deformation of the wedge are thus lower than the modern plate budget estimates (see Supplementary Note 2). This discrepancy may be caused by a combination of factors, including overestimation of the age of marker horizons R0-R5, the exclusion of the inner wedge from shortening estimates, and unaccounted additional rates from distributed shortening at sub-seismic resolutions, both in the active proto-thrust zone ahead of the frontal thrust and in older accreted equivalents. These factors have been discussed in depth in Ghisetti et al. (2016) and Barnes et al. (2018).

The restorations of the outermost part of transect ET2 (Ghisetti et al. 2016) and estimates of shortening based on a scaled analysis of proto-thrust fault displacements (Barnes et al. 2018)

give some constraints on the present-day locus of shortening in ET2. These studies show that for the past ca. 100 kyr deformation has been focused seaward of fault F14, including within the proto-thrust sequence eastward of faults F16 and F17, with nascent displacement along fault F18 on the edge of Bennett Knoll (Fig. 2a).

2.3 Décollement frictional properties along ET2: Constraints from rock mechanics experiments

The mechanical properties of sediments that host the subduction interface (décollement) strongly influence the average shear stresses that can be sustained along it, where and whether earthquakes nucleate, and how slip occurs. At shallow depths, décollement strength is dominated by frictional properties, although pressure-solution creep in phyllosilicates may also play a role (e.g., Fagereng and den Hartog, 2017; Fagereng et al. 2018). No samples yet exist for the rock units along the décollement in our study area, but in the outer part of the wedge (east of Pōrangahau Ridge) the décollement coincides with, or lies above, reflector R7, which is interpreted as the boundary between Miocene pelagic mudstones and a condensed sequence of pelagic chalks, nanno-fossil oozes and mudstones of Late Cretaceous-Oligocene age (Fig. 2a; Davy et al. 2008; Carter et al. 1999; Barnes et al. 2010; Boulton et al. 2019). An estimate of the frictional properties of these rocks may be gained from sampled analogues. Pelagic sediments recovered offshore during ODP Leg 181 at Site 1124 (offshore eastern New Zealand) comprise primarily clays (montmorillonite, illite and kaolinite), calcite, and quartz (Carter et al. 1999, 2004). Similarly, the pelagic rocks recently drilled at North Hikurangi during IODP Expedition 375 are dominated by calcite and clays, with minor quartz and feldspar (Wallace et al., 2019). Comparable rocks exposed in the East Coast region of the North Island contain the same minerals, but with modally higher illite, kaolinite, and quartz (e.g., Moore, 1988; Field et al. 1997).

The frictional behaviour of polymineralic gouge mixtures is determined by the mineralogy of the load-bearing matrix, which is mainly governed by the ratio of frictionally weak to frictionally strong minerals and gouge microstructure (e.g., Logan and Rauenzahn, 1987; Bos and Spiers, 2001, 2002; Collettini et al. 2009; Tembe et al. 2010). In pelagic chalks and clays, calcite acts as a strong phase and saturated clays are weak (Supplementary Note 3). A recent study performed at a range of plate-rate to sub-seismic slip velocities on polymineralic Miocene clayey chalk recovered from ODP Leg 181, Hole 1124C, found that the sediment exhibited a normal stress dependent friction coefficient between ca. 0.2 and 0.5 (σ_n = 1–152 MPa) (Rabinowitz et al. 2018). Other experiments on smectite clay-rich units from 1124C yielded friction coefficients as low as 0.16, although they also found that clay-bearing nannofossil chalks were frictionally stronger (friction coefficients $\mu \sim 0.35$-0.61) (Boulton et al. 2019). Regardless of gouge mineralogy, coseismic slip at high velocities ($v > 0.1$ m/s) in saturated gouges also results in very low friction coefficients of $\mu < 0.2$ because thermally activated weakening mechanisms dramatically reduce shear resistance (e.g., Faulkner et al. 2011; Ujiie et al. 2013; Bullock et al. 2015).

With increasing pressure and depth, the frictional behaviour of the décollement may become governed by the relative effects of lithification (compaction, cementation and diagenesis; e.g., Saffer et al. 2012; Trütner et al., 2015) and – potentially - fluid overpressure (e.g., Ikari et al. 2013a). The transition from smectite to illite above temperatures of ca. 120-150°C (e.g., Vrolijk, 1990) is likely to lead to an increase in frictional strength to $\mu \approx$ 0.3-0.4 or even higher if the mineral transformation reaction is accompanied by quartz or calcite precipitation (e.g., Brown et al., 2003; Saffer and Marone, 2003; Peltonen et al. 2009; Behnsen and Faulkner, 2012; Saffer et al. 2012; Trütner et al., 2015). The décollement thickness along

ET2 is unknown; based on a comparison with geological observations from ancient exhumed subduction shear zones, it likely widens to ≥ 100 m thickness with increasing pressure and temperature (e.g., Rowe et al. 2013). In the Nankai Kumano transect offshore Japan, the décollement is inferred to step downwards to the sediment-basement interface at depths of ca. 8-10 km (Park et al. 2002; Kimura et al. 2007), a transition likely driven by changes in the hydrological and/or frictional properties of the décollement (e.g., Ikari et al. 2013a). Plaza-Faverola et al. (2016) similarly suggested that along line 05CM-38 the décollement steps down ca. 2 km at depths of ca. 8-10 km just west of Pōrangahau Ridge, consequently placing it at the lowest interface between subducted sediments and Hikurangi Plateau basement (Davy et al., 2008; Ghisetti et al., 2016). The change in geometry between the inner and outer wedge may be consistent with a change in mechanical properties of the decollement west and east of Pōrangahau Ridge; there is certainly no requirement that the décollement properties (thickness, frictional strength, fluid pressure) beneath the inner wedge west of Pōrangahau Ridge should be the same as those beneath the outer wedge.

In summary, even without pore-fluid overpressure, parts of the décollement may be frictionally weak (with friction coefficients as low as ~ 0.15). With increasing temperature, the décollement is expected to become frictionally stronger as weak smectite transitions to stronger illite. This (along with changes in fluid overpressure with depth) may promote a change in the stratigraphic position of the décollement. Note that- averaged over the seismic cycle, even if sections of the décollement are dominated by stronger and velocity-weakening chalk layers, frictional weakening during seismic slip can reduce the minimum frictional strength to below ~ 0.2. Based on laboratory experiments of décollement rock analogues (and assuming saturated clays control the weakest gouge behaviour), there is a potential range in

décollement sediment friction coefficients between ~ 0.15 (low temperatures) and 0.3-0.4 (higher temperatures) even without additional weakening effects of pore-fluid overpressure.

3. Numerical experiment setup and results

Numerical experiments can be used to infer a viable range for fluid state and frictional values that are consistent with the present-day wedge morphology and deformation of transect ET2 (Fig. 2b). Such models must match geological restorations showing that the wedge is deforming mostly near its toe, with relatively lower shortening rates in the inner wedge (Section 2.2; Ghisetti et al. 2016; Barnes et al. 2018). Because the models compute rates averaged through many seismic cycles, the fluid and frictional states we infer from our mechanical analysis represent the lowest energy state (i.e., the lowest static or dynamic friction coefficients that a natural accretionary wedge would experience over a seismic cycle), since this determines the overall response of the system.

Throughout our model analyses, we refer to terms based on critical Coulomb wedge theory as outlined by Davis et al. (1983), Dahlen (1984), and Dahlen (1990.) This theory posits that an accretionary wedge deforms until it reaches a critical taper (where taper is defined as the acute angle between the surface and base of the wedge), wherein a force balance between gravitational body forces, compression from the backstop, and shear forces along the base is attained. If no further material is incorporated into the wedge, it slides stably along the base, without internal deformation. If new material is incorporated, the wedge will grow self-similarly at its critical taper value. In our study, we modify the critical wedge analysis by separating the south-central Hikurangi wedge into 2 sections (inner and outer; Fig. 2b). Mechanics in these segments is categorised as either (1) “deforming” or “sub-critical”- where the wedge taper is too low for force balance, so that it is deforming, generally by thickening

and uplifting the back of that part of the wedge; (2) “critical” where it is just in force balance- this is a transient state in mechanical models which generally transitions quickly to (3) “stable sliding”- where the wedge has attained sufficient taper to be between the upper taper limit for collapse (the angle of repose) and the lower taper limit (critical taper) so that rather than internally deforming, it slides stably over the base and transfer deformation to the more outward parts of the wedge. For small (but finite) amounts of material accreting frontally relative to the size of the wedge, a stably sliding inner and outer wedge will deform in a localised region near the toe, while over longer timescales the entire wedge will deform slowly in order to preserve critical taper.

3.1 Model Description

3.1.1 Numerical code

The numerical modelling is performed using the finite-element mechanical code SULEC which can solve for pressure-sensitive frictional deformation using an iterative yield solution to the incompressible Stokes equation for slow creeping flow (Ellis et al. 2011; Quinquis et al. 2011; Buiter and Ellis, 2012). Effects of pressure solution creep on rheology are neglected, so we do not solve for temperature. We also assume that (averaged over thousands of years) the wedge is everywhere at yield, so effects of elastic stress variations are also not computed (cf. Wang et al. 2019).

The code can model shear to >100% finite strain by using tracer particles to track strain and material parameters through the calculation (Eulerian) mesh but neglects volumetric (compressible) deformation. The brittle rheology yields according to the pressure-sensitive Drucker-Prager yield criterion, with friction coefficient and cohesion specified for each rock type. Frictional yield operates on effective mean stress (rock pressure minus fluid pressure;

Supplementary note 4). Rock pressure (mean stress) from gravitational loading and tectonic forces is calculated through an iterative penalty formulation (Pelletier et al. 1989). The Eulerian grid on which the computation is performed does not deform horizontally but stretches vertically to account for bathymetric changes at the upper surface (Fullsack, 1995). The rheology parameter values we used are summarized in Table 1.

Insert Table 1 here

3.1.2 Geometry and Boundary Conditions

We model ET2 (Fig. 2b) from x = -52 km to x = 100 km (where x = 0 is the westernmost endpoint of Transect 2 in Ghisetti et al. (2016), i.e., westward of which a detailed wedge restoration is poorly constrained by seismic reflection data). The base of the model is at 15-km depth below sea-level, while the top surface (smoothed seafloor bathymetry) is taken from Plaza-Faverola et al. (2016) and Ghisetti et al. (2016).

Velocity boundary conditions are applied at the base and left and right-hand boundaries of the model to give upper plate shortening estimates in line with those discussed in Section 2.2, although as noted there, these rates are highly uncertain. In any case, for a purely frictional (rate-independent) rheology, the exact rate of shortening is not important for analysing wedge stability. We use a horizontal velocity of v_x = 2.5 cm/yr applied at the right-hand edge and the base of the model, while we rotate this velocity vector by 3.5° along the base over a 60 km interval centred on x=0 km, so that the velocity vector remains roughly parallel to the décollement (Fig. 2b). The same velocity was also applied in a zone along the lowermost portion of the left-hand boundary, where the lower plate exits the model and subducts

westward beneath the wedge, with this velocity reduced to zero above the intersection of the décollement with the left-hand boundary, creating a backstop. The top surface is a free boundary, although a pressure load is applied to it to represent the weight of overlying seawater.

We use the present-day wedge geometry and inferred material distribution as the initial condition and run the mechanical code forward in time for 5 timesteps of 1000 years duration (i.e. a total relative convergence across the transect of 125 m). This predicts the present-day stress field and the average mechanical response of the system on a time scale that is long enough to be averaged over several seismic cycles (since the average return period for large Hikurangi subduction earthquakes is ca. 700 years; Clark et al., 2019), but short enough to neglect changes in sediment accumulation or subducting ocean floor topography (Fig. 2b). We do not consider transient changes associated with the earthquake cycle. For this reason, the frictional parameters may be viewed as those controlling mechanics over many seismic cycles.

3.1.3 Fluid state

The models do not include fluid flow, but incorporate fluid pressure (P_f) effects using the generalized fluid overpressure ratio to vertical lithostatic load σ_z, $\lambda = (P_f - \rho_f g D)/(\sigma_z - \rho_f g D)$ where ρ_f is fluid density, g is gravity, and D is the depth of the wedge below sea-level, so that $\rho_f g D$ is the weight of the overlying water column (Davis et al. 1983). We specify different values for fluid overpressure ratio along the basal décollement (λ_b) and as a depth-averaged value within the wedge ($\hat{\lambda}_w$) (Skarbek and Rempel, 2017). They showed that if the fluid overpressure ratio increases linearly in a wedge from the seafloor to the décollement, this average wedge fluid overpressure $\hat{\lambda}_w = [2\lambda_b + \lambda_h] / 3$, where λ_h is the hydrostatic fluid pressure ratio at the seafloor.

By making these simple assumptions, the models can investigate the range of λ_b and $\hat{\lambda}_w$ for which the wedge is critical and stable, vs. when it is sub-critical and internally deforming.

3.1.4 Sediment properties: A hierarchy of model experiments

Ideally, each sediment unit within the outer wedge shown on Fig. 2a - where the litho-stratigraphic boundaries are reasonably well-constrained - would be modelled separately using physical properties and frictional parameters constrained by borehole data and rock mechanic experiments. Since these data are unavailable for the study area, in our base models (P1 and P2) we simply assume that the whole sedimentary package in the wedge has an average friction coefficient (μ_w) of 0.8 and a small cohesion (C) of 1 MPa. This assumption allows us to check our results against analytical predictions from cohesion-less critical Coulomb wedge theory (Dahlen, 1984) and to compare results with previous models of Hikurangi wedge stability. For example, Fagereng (2011) assumed a wedge friction coefficient $\mu_w = 0.8$ and basal friction coefficient $\mu_b = 0.3$ and varied fluid pressure ratio for equal wedge and basal fluid pressure ratios ($\lambda_b = \hat{\lambda}_w$). Similarly, and following the range outlined in Section 2.3, we impose uniform material properties along the décollement, with two choices for the décollement friction coefficient: $\mu_b = 0.15$ (Ujiie et al. 2013; Bullock et al. 2015; Morrow et al. 2017) and $\mu_b = 0.3$ (Ikari et al. 2009a, 2009b; Fagereng, 2011; Rabinowitz et al. 2018). In models P1 and P2 (described below) we use a constant porous sediment density of 2500 kg m^{-3} for unlithified low-cohesion sediments, consistent with a value that can be calculated using an exponential decrease in porosity with depth (Sclater and Christie, 1980) taking the depth coefficients from Ghisetti et al. (2016), assuming a typical wedge sediment burial depth of 3 km, average porosity of 15%, and a solid rock density of 2675 kg m^{-3}. Model P3 addresses the expected increase in bulk density (Skarbek and Rempel, 2017) and cohesion (Schumann et al. 2014) with burial depth and compaction, by imposing a

density which increases with depth below seafloor, and cohesion that depends on effective mean stress. Models P4 and P5 also explore changes in décollement friction (model P4) and geometry (model P5) with depth.

The sections below outline the results for a series of models that test present-day wedge stability by progressively adding more features based on the present-day wedge structure described in Ghisetti et al. (2016) and Plaza-Faverola et al. (2016).

3.2 Results for Model P1- uniform wedge and décollement friction

Our first model neglects the weakening effect of faults in the wedge and has constant bulk density. We firstly set the friction parameters of sediments and of the basal décollement to be constant and vary their fluid pressure ratios to determine how much of the wedge is stable (i.e. able to propagate forward without internal deformation) vs. compressionally unstable (i.e. undergoing shortening and uplift). We use a dry wedge coefficient μ_w = 0.8 and basal décollement friction coefficient μ_b= 0.15 or 0.30 (Table 1). Three modes of wedge behaviour – based on patterns of vertical uplift, strain-rates, and deformation- are observed in model P1 (Fig. 3), in agreement with predictions from critical wedge theory when a change in basal dip is incorporated (Davis et al. 1983; Dahlen, 1990; Fagereng, 2011). For a very weak basal strength, where basal friction is low and/or basal fluid pressure is close to lithostatic, the wedge is stable everywhere and deforms at its toe (mode 1; Fig. 3a). For intermediate basal friction and/or fluid pressures, the larger taper of the inner wedge allows it to be critical and/or stable (e.g., Dahlen, 1990), while the outer wedge is subcritical and shortens against the inner wedge by uplift above the change in basal dip (mode 2; Fig. 3b). When basal friction is high and/or fluid pressures are hydrostatic, giving high basal effective strength

relative to the wedge, the inner wedge is below critical taper and grows against the backstop at the left-hand side of the model (mode 3, Fig. 3c).

Insert Fig. 3 here

The influence of fluid pressure may be summarised by plotting the three wedge modes of Fig. 3 as a function of fluid pressure ratios in the wedge and basal décollement, using graphs that plot λ_b vs. $\hat{\lambda}_w$ (Fig. 4a). Each dot represents a P1 model result for a specified set of λ_b and $\hat{\lambda}_w$ values. The region of intermediate stability between the inner and outer regions of the wedge (mode 2 on Fig. 3) is shaded in grey. Predictions from critical wedge theory for a cohesion-less wedge are also shown, where the two lines are for wedge taper of 4° and 2° (lines respectively labelled inner and outer wedge). These lines (Fig. 4a) highlight an important distinction between the inner and outer wedge based purely on geometry. While both inner and outer wedges have an average surface slope of ca. 0.5-1°, the basal dip of the outer wedge décollement is only 1°, giving a taper angle of 2°, while the basal dip of the inner wedge décollement is ca. 3.5°, giving a taper angle of 4° (Fig. 2b). This difference in taper means that – for a given effective frictional strength in the wedge and along the décollement - the inner wedge is closer to a critical force balance, and will reach criticality more readily than the outer wedge, resulting in stable sliding (e.g., Dahlen, 1990). The model predictions for intermediate wedge stability shown in Fig. 4a (grey shaded region) are in rough agreement with the inner and outer wedge predictions from non-cohesive critical wedge theory (black and red lines). The deviation from cohesionless critical wedge predictions is greatest for very high fluid pressure ratios in the wedge and along the décollement.

When basal fluid pressure ratio λ_b is low, the wedge is unstable even at a taper of 4° and the inner wedge undergoes internal deformation (e.g., black dots on Fig. 4a, corresponding to the

model from Fig 3c). For intermediate λ_b, the outer wedge is subcritical and deforms (purple dots on Fig. 4a, corresponding to the model from Fig. 3b). For sufficiently high λ_b, the entire wedge is stable, and deformation is focused at the toe and along the décollement (red dots on Fig. 4a, corresponding to model from Fig. 3a). The model also predicts a range of possible fluid overpressures in a region of intermediate stability between a completely subcritical wedge (that grows at the rear) and a wedge that is completely stable (that will propagate forward, with deformation localised at the toe). For intermediate stability, a combination of modes is possible (black-in-purple and red-in purple dots).

When the décollement has a weaker friction coefficient of 0.15, the décollement fluid pressure ratio required to attain critical taper is lower (Fig. 4b). The theoretical stability lines (red and black lines) for 2° and 4° tapers shift downwards, and this effect is also seen in the model results (red, purple and black dots). Thus, when the décollement is frictionally very weak, a very low-taper wedge can develop with uniform, and near-hydrostatic, fluid pressure ratios within the wedge and décollement (Fagereng, 2011). To illustrate this further, Fig. 4c and d show stability results where fluid pressure ratios are constant and equal in the wedge and décollement ($\lambda_b = \hat{\lambda}_w = 0.4$ in Fig. 4c and $\lambda_b = \hat{\lambda}_w = 0.7$ in Fig. 4d) while basal and wedge friction coefficients vary. As predicted by critical wedge theory, for a given average wedge friction coefficient and constant fluid pressure ratios, a lower décollement friction allows the wedge to slide stably with localised deformation at its toe.

Insert Fig. 4 here

3.3 Results for Model P2- Influence of weak faults in the wedge

The litho-stratigraphic units shown in the transect of Fig. 2a have been offset along numerous thrust faults with displacements exceeding 1.5 km (Ghisetti et al. 2016). Faults can alter the force balance within a critical wedge, since the bulk strength of the wedge is controlled by its weakest part (e.g., Lohrmann et al. 2003). The effect that faults have on wedge dynamics is shown in model set P2, where the faults shown on Fig. 2 are added and given a friction coefficient of 0.55 and cohesion of 0.1 MPa – i.e. intermediate between undeformed wedge sediment and the basal décollement friction and cohesion values. In this simple model, faults are assumed to have the same fluid pressure as surrounding wedge material, but for many of the faults of the offshore Hikurangi margin there is evidence for fluid flow (e.g., Barnes et al. 2010; Pecher et al. 2010;) which may indicate higher fault fluid overpressures at depth, at least transiently.

Fig. 5a-b shows the range of stable, intermediate, and unstable wedge fluid ratios where the faults are included. The model results (coloured dots) show that the stable zones are shifted up relative to the critical wedge predictions for no faults (dashed red and black lines, Fig. 5a-b)- meaning that a higher basal overpressure is required (for a given wedge overpressure ratio) to make the wedge stable. The zone with intermediate modes (grey shading) is also shifted up. This is unsurprising, since the inclusion of weak faults decreases the strength ratio between the wedge and basal décollement (e.g., Lohrmann et al. 2003), making it easier to deform the wedge internally rather than propagate the wedge forward. However, the faults only partially weaken the wedge compared to a case where the whole wedge is composed of fault material (solid red and black lines, Fig. 5a-b). The progressive effects of fault weakening is demonstrated for a specific model example in Fig. 5c.

Insert Fig. 5 here

3.4 Results for Model P3- effect of increasing density and cohesion with depth

In model P3 (Table 1), we repeat the analysis from model P1 (Fig. 4) but prescribe cohesion and density values to increase with depth (Fig. 6a). Porous sediment density ρ is calculated by taking a solid density of 2675 kg m^{-3} and water density of 1000 kg m^{-3} to give:

$$\rho = (1 - n)(2675) + n(1000)$$

where n is calculated porosity, which decreases exponentially with depth (Sclater and Christie (1980)). We use compaction parameter values from Ghisetti et al. (2016):

$$n = n_0 \exp(-cz)$$

where n_0 is 0.6, c is 0.5 and z is depth in km. We also impose an increase in cohesive strength C with depth, using values based on Schumann et al. (2014), who compared frictional properties of mudstone samples from the inner, consolidated paleo-accretionary complexes of SW and central Japan and samples from the shallow frontal toe of the modern accretionary prism at Nankai. They found friction coefficients to remain approximately constant (ca. 0.6-0.7) with depth, but cohesion increasing with maximum burial depth. They compiled a range in cohesion with depth from < 1 MPa at the toe of the modern accretionary prism (Lempp et al. 2010) to between 13 and 30 MPa at 9 km depth.

We prescribe cohesion to increase linearly with depth, from a lower limit of 0.1 MPa near the seafloor to a maximum of 22 MPa (the median cohesion measured at Shimanto; cf. Schumann et al. 2014) for ≥ 9 km depth. We set the décollement friction coefficient to 0.3 (Table 1). In the first set of P3 models, faults are given the same friction coefficient and cohesion as the wedge (cf. Fig. 4). Note that since sediment density is increasing with depth,

fluid pressure ratio $\hat{\lambda}_w$ is no longer constant and is higher than its average value close to the seafloor.

Model results (Fig. 6b, c) indicate that the increase in density and cohesion with depth has only a minor effect on wedge stability, with the greatest effect coming from the increasing cohesion. Fig. 6b shows that, for a case with no weak faults, it is slightly easier to stably slide the inner wedge with no deformation but slightly harder to stably slide the outer wedge compared to the case with a constant cohesion and density (Fig. 4a- zone of intermediate stability also shown by grey dashed lines on Fig. 6b). That is, for a given set of friction coefficients and wedge fluid overpressure ratio, a slightly lower fluid pressure is required to promote stable sliding along the inner décollement (where cohesion is highest) compared to the case with a low and constant sediment cohesion.

In a second set of P3 models, where weak, low-cohesion faults are present in the wedge, this effect is reversed- i.e., it becomes harder to make the inner wedge slide stably, and greater fluid overpressures are required along the inner décollement (Fig. 6c). Since the contrast between the weak, low cohesion faults and surrounding wedge material is greatest at the back of the wedge, relatively more fault weakening occurs there compared to the outer wedge, which has a low cohesion anyway (Fig. 6c cf. Fig. 5a).

Insert Fig. 6 here

3.5 Results for Model P4- increasing décollement strength with depth

As discussed in Section 2.3, the transition from smectite to illite with increasing temperature and pressure can increase clay-dominated friction coefficients from ~ 0.15 to 0.3-0.4. To test the effect this has on wedge stability, we modified model P3 (with increasing cohesion and

density with depth) by imposing a basal décollement friction coefficient for the outer wedge of μ_{bo} = 0.15 and inner décollement friction coefficient μ_{bi} = 0.3. This collapses the theoretical critical wedge stability limits toward each other (Fig. 7a red vs black lines) and introduces a new mode where the entire wedge is near-critical ("entire wedge deforms" mode, Fig. 7a and 7b).

Insert Fig. 7 here

3.6 Results for Model P5- Effect of a stepdown in the décollement

Plaza-Faverola et al., (2016) interpreted the subduction interface on seismic line 05CM-38 as a shallow dipping thrust that steps down ca. 2 km beneath Pōrangahau Ridge to the base of the subducting sediment zone along an 18 km wide ramp. We tested the effect such a step-down in the décollement would have on present-day wedge mechanics, using the step-down geometry shown on Fig. 8b-c, where- in addition to the upper décollement (model P3)- a lower décollement is imposed at the interface between subducting sediment and the subducting plate (Hikurangi Plateau basement). In the model, this lower décollement is only present from the left-hand backstop eastward to the interface beneath Pōrangahau Ridge. The left-hand boundary condition is adjusted to force sediment above the lower décollement to become part of the wedge instead of subducting (i.e., $v_x = v_y = 0$ above the lower decollement at the left-hand boundary).

Fig. 8 illustrates the effect of this lower décollement for a wedge that is otherwise just approaching conditions for mode 1, with uplift split between the outer wedge and the wedge toe. Comparison between the case with a smooth décollement (no stepdown, Fig. 8a) and the case where both the top and bottom of the subducting sediment have weak regions that can

detach (Fig. 8b) demonstrates that- even if a step-down is present- it does not necessarily lead to enhanced uplift above it. Focused uplift only occurs when the transition is abrupt (e.g., Fig. 8c, where the upper weak layer ends landward of Pōrangahau Ridge).

Insert Fig. 8 here

4. Discussion

4.1 Implications of our results for present-day wedge state

The numerical models described in Section 3 verify- and extend- observations obtained from previous analyses of the Hikurangi margin. Fagereng (2011) assumed a wedge friction coefficient of 0.8 and a minimum basal décollement friction coefficient of 0.3. He analysed stability for the inner wedge taper of 4°. Given the same fluid pressure conditions on the décollement and the wedge ($\lambda_b = \hat{\lambda}_w$), he found that a stable inner wedge was only possible for high fluid pressures, requiring a basal décollement fluid overpressure of at least 0.9, i.e. nearly lithostatic. Our analysis shows that for the same conditions, even higher fluid overpressures would be required in the outer wedge, where the taper is only 2°. Furthermore, weakening of the overlying wedge by faults would make it impossible to create a stable wedge without $\lambda_b > \hat{\lambda}_w$, since weak faults shift the required basal fluid pressure ratio (for stable sliding) upward (Fig. 5a, 6c).

However, Fig. 4 - 7 show that there is a range of fluid overpressure ratios and friction coefficients beyond those explored by Fagereng (2011) that allows the wedge to be critical or

slide stably with deformation focused at the toe. This requires either relaxing the condition that $\lambda_b = \hat{\lambda}_w$, and/or that décollement friction coefficient is the same at all depths.

If the average wedge fluid pressure ratio is less than the fluid pressure ratio along the décollement, the range of permissible fluid pressure ratios along the décollement expands considerably. Even for constant friction coefficients, moderate décollement fluid overpressure ratios of 0.7 can still create a wedge with the observed taper that is mostly stable and deforming at the toe. If the décollement friction coefficient is low (e.g., $\mu_b = 0.15$; Fig. 4b) the required décollement fluid overpressure need be only slightly higher than hydrostatic ($\lambda_b \geq 0.47$, without weak faults in the wedge- Fig. 4b; or $\lambda_b \geq 0.55$, with weak faults- Fig. 5b) and the wedge will be critical and propagate forward at its toe.

Moreover, from Fig. 4a cf. 4b, we note that a wedge can be stably sliding at low to moderate fluid pressures even with a décollement friction of 0.3 beneath the inner wedge, because of the higher taper angle there. Setting the outer décollement friction coefficient $\mu_{bo} = 0.15$ (e.g., Bullock et al. 2015; Morrow et al. 2017) and inner décollement friction coefficient $\mu_{bi} = 0.3$ (e.g., Fagereng, 2011; Rabinowitz et al. 2018) allows both inner and outer wedges to be critical with λ_b only slightly higher than the average fluid overpressure ratio in the wedge, $\hat{\lambda}_w$ (e.g., for hydrostatic wedge fluid pressure, $\lambda_b \geq 0.6$; Fig. 7). It is quite plausible that the outer décollement has a low frictional strength dominated by weak smectite layers (Saffer and Marone, 2003; Moore and Lockner, 2007; Ujiie et al. 2013; Rabinowitz et al. 2018; Boulton et al., 2019), while the inner décollement at greater depths may have a higher effective strength due to diagenetic reactions, transformation of smectite to illite, cementation and/or localisation in different lithologies (e.g., Moore and Saffer, 2001; Moore et al. 2007; Peltonen et al. 2009; Trütner et al., 2015; Section 2.3). It is also possible that fluid overpressures along the outer décollement are higher than those at the inner décollement, owing to compaction

disequilibrium during initial loading and porosity loss and the lack of permeable pathways (e.g., Saffer and Tobin, 2011; Lauer and Saffer, 2012; Ellis et al., 2015).

4.2 The effect of weak faults and lithification on wedge stability

As Fig. 5 illustrates, weak faults within the wedge can cause the entire wedge to be subcritical i.e. be deforming internally, while the same model that has no faults is critical or stable (e.g., Lohrmann et al. 2003). Anything that weakens the wedge requires a weaker basal strength to propagate forward at critical or stable taper, compared to a stronger wedge. Besides the influence of weak upper plate faults, high fluid pressure in the wedge can cause it to deform subcritically compared to the equivalent (critical) case with a drained wedge. The wide distribution of active fluid seeps on thrust ridges within the middle and inner wedge near the study area (Barnes et al. 2010; Greinert et al. 2010; Pecher et al. 2010; Plaza-Faverola et al. 2014) may indicate that the inner part of ET2 is at least partially drained by fluid flow along faults, keeping it sufficiently strong relative to the basal décollement, and resulting in a critical wedge. On the other hand, inner wedge overpressure at depths > 1.5 km is observed in a nearby industry well (Titihaoa-1; south of ET2; Fig. 1) (Darby and Funnell, 2001; see also Burgreen-Chan et al. 2016).

Model results summarised in Fig. 4 and 5 were constructed assuming low and constant cohesive strength in the wedge, and mostly matched results from non-cohesive critical wedge theory. Sediment strength and density are expected to increase with burial depth owing to compaction and diagenesis (e.g., Peltonen et al. 2009; Lauer et al. 2017), and in accord with increasing p-wave velocity (Plaza-Faverola et al. 2016). This increase may affect wedge stability (e.g., Zhao et al. 1986). Skarbek and Rempel (2017) derived correction factors to represent effects of decreasing porosity (and therefore, increasing bulk density) and found

that an exponential decrease in porosity with depth reduces the shear traction required along the base of the wedge to attain criticality. In Model P3 (Fig. 6) we found that a stronger, more cohesive wedge permits a higher effective basal strength while allowing the inner wedge to slide stably and deform. However, weak faults reverse the effect of increasing cohesion on wedge taper, since – when present- they dominate the stability of the wedge, particularly when they have a very low cohesion compared to surrounding wedge material in the inner wedge (e.g., Lohrmann et al. 2003); (Fig. 6c).

In this paper we have assumed a constant wedge friction coefficient of 0.8, to facilitate comparison with earlier studies such as Fagereng (2011). It could be argued that the unlithified sediment in the outer wedge- as well as having a lower cohesion as discussed above- may also have a reduced friction coefficient (e.g., Ikari et al. 2013a; Trütner et al., 2015; Wang et al. 2019). If so, this makes it even harder to propagate deformation to the toe of the wedge. For example, if all sediment above reflector 7 (Fig. 2a) is given a reduced friction coefficient that is the same as the faults (μ_{wo} = 0.55) the zone of intermediate wedge stability expands, and relatively higher basal fluid pressures are required to match present-day deformation (Supplementary Fig 1) compared to the case with uniform wedge friction (Fig. 7a). Even so, a stable and forward propagating wedge is still compatible with moderate (sub-lithostatic) décollement fluid overpressures of λ_b ~ 0.7-0.8 and hydrostatic wedge fluid pressures ($\hat{\lambda}_w$ ~ 0.4).

4.3 Deriving physical conditions within the present-day south-central Hikurangi wedge

An objective of our analysis was to derive a set of consistent and physically realistic conditions for stress, fluid pressure, wedge sediment, and décollement properties to reproduce the present-day wedge structure. The numerical models illustrate the trade-off between

décollement frictional strength, the strength and cohesion of upper plate faults in the wedge, and fluid pressure, and show that there is a defined range of plausible values for these parameters that can explain the present-day wedge taper and present-day shortening concentrated near the toe. The higher the fluid overpressure is in the wedge sediments, the higher the fluid overpressure along the basal décollement must be to attain a stable or critical taper, allowing deformation to be focused at the wedge toe without high rates of deformation and shortening in the inner parts of the wedge. The model results for homogeneous wedge properties verify predictions from critical wedge theory for low to moderate fluid overpressures, though they deviate at high fluid overpressures (> 80%) in the low-taper, outer wedge.

Even when neglecting the effect of weak upper plate faults and assuming uniform material properties in the wedge and along the décollement, there are four potential parameters that can influence wedge stability: wedge and décollement fluid overpressure ratios; and wedge and décollement friction coefficients. For near-hydrostatic fluid pressures and Byerlee-type frictional strength in the wedge, Fig. 4c shows that a very low décollement friction coefficient of $\mu_b \leq 0.15$ is necessary to focus deformation at the wedge toe. An even weaker décollement is required for a stable wedge if weak upper plate faults are included in the analysis (Fig. 5; section 4.2). In any case, the *effective* strength of the décollement must be quite weak to explain the overall low taper of the wedge, as noted in previous studies (e.g., Fagereng, 2011; Skarbek and Rempel, 2017) and in line with some global estimates from subduction margin surface heat flow constraints (e.g., Gao and Wang, 2014; England, 2018).

The choice and combination of parameter values is of course non-unique, but for a given fluid overpressure ratio in the wedge, with weak faults in the inner (consolidated) wedge material and assuming the inner décollement has a higher friction coefficient than the outer décollement, Fig. 7 can be used to estimate the fluid pressure ratios along the décollement

necessary to maintain the observed taper. For example, if $\hat{\lambda}_w = 0.6$, then λ_b must be ≥ 0.7 for wedge stability. The geological interpretation of section ET2 (Fig. 2) indicates that the wedge has only propagated to the outermost fault F18 in the Late Quaternary and that many of the inner faults may still be active (e.g., Stirling et al. 2012), suggesting that the faults are weak, and the wedge is likely to be near criticality everywhere (e.g., Fig. 7b). For a uniform, moderate fluid pressure ratio within the wedge ($\hat{\lambda}_w \sim 0.6$), a critical or stable state can be imposed by (1) assigning the same friction coefficient (e.g., $\mu_b = 0.3$) everywhere along the décollement, but varying the fluid pressure ratio (e.g., from $\lambda_{bi} > 0.65$ in the inner décollement to $\lambda_{bo} > 0.85$ in the outer décollement; Fig. 6c); or, (2) maintaining $\lambda_b \approx 0.7$ everywhere, but giving a lower friction coefficient to the décollement clays in the outer wedge (Fig. 7). Another way to visualise these choices is shown in Fig. 9, where average wedge fluid overpressure is assumed to be (a) hydrostatic or (b) between hydrostatic and lithostatic, and the required sediment friction coefficient vs. required (minimum) décollement fluid overpressure is plotted. Outer and inner wedges have been separated (blue vs. red curves). The plots show that a décollement dominated by smectite clays such as saturated montmorillonite is weak enough to account for the low outer wedge taper even at reasonably low basal fluid pressure ratios of $\lambda_b \approx$ 0.5-0.6, provided the overlying wedge is relatively strong (i.e., it does not have high fluid pressures). Even a stronger frictional décollement dominated by illite (as expected at greater temperatures and pressures) can be weak enough to account for stable sliding of the inner wedge, for a hydrostatically-pressured wedge (Fig. 9a). However, if the wedge above the décollement is weaker (for example, if it is moderately overpressured as in Fig. 9b, and/or has a lower friction coefficient due to the presence of a weak clay fraction or weak faults), stable sliding of the inner wedge becomes more difficult. In that case, a weaker friction coefficient and/or high fluid pressure along the décollement (λ_b > ca. 0.7) is required to maintain a shallow taper (Fig. 9b).

Insert Fig. 9 here

4.4 Continuity of the décollement from the inner wedge to the toe

Plaza-Faverola et al. (2016) used prestack depth migration data on seismic line 05CM-38 to derive seismic velocities and interpret subducting plat geometry and upper crustal structure to ca.14 km depth. The inferred 2-km vertical step-down in the décollement beneath Pōrangahau Ridge was interpreted to be associated with a cluster of splay faults in the upper plate, and with the zone of maximum slip (90 mm) interpreted to have occurred on the subduction interface during slow slip events in June and July 2011 (Plaza-Faverola et al. 2016).

Our tests of a step-down in the décollement (Model P5) show that its effect on present-day wedge mechanics depends on the length-scale over which the stepdown occurs (Fig. 8). A sharp transition produces a zone of localised stress transfer from lower to upper plate and focused uplift which is not consistent with present-day geometry and shortening estimates from restoration of the wedge (e.g., Ghisetti et al. 2016). This suggests, if there is a step-down, that the configuration resembles Fig. 8b, where enhanced deformation steps downward over a wide zone of distributed shear, such as might be expected within a subduction channel or mélange (e.g., Shreve and Cloos 1986; Moore and Byrne 1987; Kimura et al. 2007). While further modelling is required to test the long-term effects of such a transition on wedge development over millions of years, significant sediment underplating in this region is not compatible with the low uplift rates inferred from reconstructions (Ghisetti et al., 2016). However, as pointed out by as Plaza-Faverola et al. (2016), mélange-style mechanics may promote slip and stress transients with transient high fluid pressures there (e.g., Fagereng and

Sibson, 2010; Webber et al. 2018; Beall et al. 2019). While our stability analysis rules out a sharp step in the level of the décollement, even a gradual step-down may influence the seismogenic potential of the subduction interface (e.g., Kimura et al., 2007; Ikari et al. 2013a; van Rijsingen et al., 2018). Kimura et al. (2007) analysed Nankai accretionary wedge structures and seismic profiles and suggested that the location of a step-down in the décollement may be mechanically linked to either: (1) the change in wedge taper (with higher taper angles for the inner wedge); (2) the presence of out-of-sequence thrust faults; and/or (3) and the up-dip limit of the seismogenic zone. Along ET2, the conjectured step-down location is roughly coincident with the transition from outer to inner wedge geometry (e.g., Fig. 2a) and the presence of faults (F9 to F12) that have accrued additional displacement within the last few hundred thousand years (Ghisetti et al., 2016). Alternatively, these changes may reflect a transition in décollement properties rather than a step-down, as discussed in Section 4.3.

4.5 Is the south-central Hikurangi wedge critical everywhere?

Wang et al. (2019) used earthquake focal mechanisms from the 2011 M_w 9 Tohoku-oki earthquake, force balance models, and dynamic Coulomb wedge theory (which considers stress changes during earthquake cycles; Wang and Hu, 2006) to demonstrate that when effective basal strength is very low, a wedge can flip from a compressive critical to an extensional critical state very easily- i.e., it may attain critical state only transiently during the seismic cycle. Their results support the interpretation that the inner wedge above the Japan Trench plate boundary is stable and well below yielding, while the outer wedge is mostly stable but occasionally enters a critical state during great earthquakes.

While we are modelling a specific time snapshot here- the present-day force-balance of the south-central Hikurangi margin- we consider long enough timescales to average effects from multiple seismic cycles over which permanent deformation accrues. We have shown that a state where the inner wedge can slide stably with little deformation, while the outer wedge and/or toe are deforming, is relatively easy to achieve. To match the present-day locus of deformation in the outer wedge, we predict effective outer wedge basal friction coefficients (including the effects of fluid pressure, i.e., $\mu' = \mu(1-\lambda)$) of ~ 0.03-0.09, which are similar to the values calculated by Wang et al. (2019) for Tohoku. One difference is that (unlike the prominent Japan subduction trench), the structures illustrated on transect ET2 show no trench where the décollement breaks the seafloor (Fig. 2a); instead, the toe of the prism gently abuts the incoming Bennet Knoll seamount and deformation is absorbed in a more distributed fashion on a few low-displacement thrust faults and within a protothrust zone that cut through a ~ 3-4 km-thick sediment package (Ghisetti et al. 2016; Barnes et al. 2018). For these reasons we think it unlikely that south-central Hikurangi will experience the same coseismic slip behaviour as that observed at Tohoku in 2011. Further (short-term) models that incorporate earthquake rupture and earthquake stress cycling are needed to fully explore these differences.

4.6 Comparison between the southern and northern Hikurangi wedge

Present strain accumulation measured by geodesy demonstrates a transition from a mostly creeping subduction plate interface (northern Hikurangi margin; Fig. 1a) to an interseismically-locked subduction interface along the south-central Hikurangi margin (Wallace and Beavan 2010; Wallace et al. 2012). Reasons for this transition are still debated (Wallace et al. 2009). Compared to south-central Hikurangi, northern Hikurangi has a higher

trench convergence rate (up to ca. 60 mm/yr), a reduced thickness of accreting sediment (< 1.5 km), an increase in roughness of the subducting plate hosting more subducting seamounts, and thinner, less buoyant Hikurangi Plateau crust (Lewis and Pettinga, 1993; Wood and Davy, 1994; Davy et al. 2008; Barker et al. 2009; Wallace et al. 2009; Barnes et al. 2010). The north also has a much steeper frontal taper (>10°) than the south. These changes may result from variations in lithological and frictional strength (e.g. Saffer and Marone 2003; Boulton et al., 2019), increased roughness of the subducting plate to the north (e.g, Dominguez et al. 2000; Ellis et al. 2015) and/or variations in porosity and fluid pressure (Fagereng and Ellis, 2009; Bell et al. 2010; Bassett et al. 2014; Ellis et al. 2015; Saffer and Wallace, 2015; Skarbek and Rempel, 2017).

The critical wedge analyses of Fagereng (2011) and Skarbek and Rempel (2017) predict a stronger basal décollement beneath the steep outer taper of the northern Hikurangi wedge, compared with the weak basal décollement predicted for south-central Hikurangi. Provided the frictional strength of the décollement rocks do not change significantly along-strike, this requires that the northern Hikurangi décollement has less fluid overpressure compared to south-central Hikurangi (e.g., Fagereng and Ellis, 2009; Fagereng, 2011). However, Skarbek and Rempel (2017) pointed out that the wedge in northern Hikurangi may not be in a critical stress state, in which case it may be over-steepened relative to its equilibrium taper angle, thus allowing higher décollement fluid pressure in the north. This is consistent with other geophysical interpretations suggesting high fluid pressure in the north, such as slower wave speeds (Bassett et al. 2014); high *Vp/Vs* seismic velocity ratios with strong P-wave attenuation (Eberhart-Phillips et al. 2005, 2008; Reyners et al. 2006; Eberhart-Phillips and

Bannister, 2015); zones of higher seismic reflectivity on or near the subduction interface (Bell et al. 2010); and predictions from fluid-flow models (Ellis et al. 2015).

In Figure 10 we schematically compare the key features of northern vs. south-central Hikurangi wedges, using depth converted seismic line 05CM-04 in the north (Fig. 1a; Barker et al. 2009, 2018; Bell et al. 2010; Ellis et al. 2010; 2015) and transect ET2 from this paper in the south. While many of the features in Fig. 10 are speculative, in general the northern wedge has a higher and more variable taper, resulting from recent seamount subduction beneath the margin (Barker et al. 2018). Critical wedge equilibrium is not expected in the region, because the wedge responds transiently to the seamount passing below it, creating a flat top and steep frontal taper with a splay fault (e.g., Dominguez et al. 2000; Ellis et al. 2010; Morgan and Bangs, 2017).The northern Hikurangi wedge also includes several splay faults, some of which appear to intersect the interface in regions of low interseismic coupling (Mountjoy and Barnes, 2011). These splay faults may allow transient deformation and fluid flow (e.g., Shaddox and Schwartz, 2019). As a result, it is hard to infer the degree to which fluid overpressure is present in the northern wedge and/or along the basal décollement from analysing current wedge taper, as neither the taper nor the fluid pressure state is likely to reflect a steady state. The presence of bright reflectors and aseismic creep at depths as shallow as 15 km, accompanied by slow-slip reaching to very shallow levels, possibly to the trench (Wallace et al. 2004; Wallace et al. 2016), has been attributed to potentially higher (near-lithostatic) plate interface fluid pressure and/or more lithological heterogeneity there, in comparison to our study area (Fagereng and Ellis, 2009; Wallace et al. 2009; Bell et al. 2010; Bassett et al. 2014; Eberhart-Phillips and Bannister, 2015; Ellis et al. 2015; Saffer and Wallace, 2015). Numerical calculations for northern Hikurangi predict regions with substantial overpressure generated by porosity loss in the subducting sediments (Ellis et al. 2015). In addition, transient changes in fault slip styles, including slow slip, tremors,

earthquakes, and tsunamigenic earthquakes (Bell et al. 2010, 2014; Wallace et al. 2016; Todd et al. 2018; Shaddox and Schwartz, 2019) could reflect spatial and temporal fluid pressure and material heterogeneities (Kano et al. 2018).

In contrast to the north, the south-central wedge has features that are consistent with a critical wedge. The numerical model results from Section 3 show that there is a trade-off between wedge strength and the strength of the basal décollement to achieve criticality; but considering the low frictional strength of décollement zone phyllosilicates, we suggest that the south-central wedge may be only moderately overpressured, with a moderate (inner wedge) to high (outer wedge) fluid overpressure along the plate interface. If the shallow basal décollement is controlled by a smectite phyllosilicate rheology transitioning to frictionally stronger clays at depth, then the wedge can be critical with moderate overpressure (ca. 40-60% lithostatic) in the wedge, moderate overpressure on the décollement beneath the inner wedge (ca. 45-65% lithostatic), and higher fluid overpressure beneath the outer wedge (ca. 60-80% lithostatic; Fig. 7). Higher fluid pressures along the outer wedge décollement are consistent with enhanced compaction-related fluid sources during loading by the overlying wedge (e.g., Ellis et al., 2015), and because of the relative immaturity of faults in the outer wedge- i.e., a lack of well-developed, high-displacement faults with permeable damage zones acting as connected fluid pathways- may allow higher décollement fluid pressures to be maintained there, since networks of small-scale fractures in the fault damage zones and in the protothrust zone are unlikely to provide a continuous fluid pathway to the surface.

Insert Fig. 10 here

5. Conclusions

In this paper we have used numerical models of an interpreted south-central Hikurangi transect to investigate admissible wedge and décollement friction strength and fluid pressure conditions for a wide, low-tapered accretionary wedge. Physically realistic parameters for fluid pressure, and sediment and décollement friction based on laboratory experiments of weak phyllosilicates, have informed numerical models which are able to reproduce the present-day mechanics of the south-central Hikurangi wedge (transect ET2, based on seismic lines CM05-38-SO-191-4), with deformation currently focused near the toe of the wedge.

A wedge stability analysis of the present-day accretionary wedge points to either high to moderate fluid pressure on the plate interface, and/or or weak friction along the décollement to explain the present-day taper. The outer wedge décollement is predicted to have a weaker effective strength than the décollement beneath the inner consolidated wedge material. As predicted by previous studies, we have verified that the presence of weak faults in the wedge requires a weaker décollement and/or higher fluid pressure along the décollement to maintain the present-day taper, compared to the case where faults are not included in the models.

We have also investigated the effect of variations in material properties with depth. For the same friction values and fluid pressure ratios, increasing density and cohesion with depth make it slightly easier for the inner wedge to attain a stable taper. If a second, lower weak layer is present at the top of the subducting plate beneath the inner wedge, it can cause a stepdown in the décollement beneath Pōrangahau Ridge. While this stepdown can explain conditions leading to ridge uplift, such uplift does not influence wedge mechanics significantly unless the step-down is unrealistically sharp. The effects such a stepdown would have on limiting the extent of earthquake rupture and continuity of interface slip remains to be investigated.

In comparison to the northern Hikurangi wedge, which is unlikely to be in critical force balance, south-central Hikurangi can be at or near critical wedge equilibrium with moderate fluid pressures (even hydrostatic) in the wedge, provided there are moderate to high fluid overpressures along the basal décollement. Our results suggest that the low taper observed in wedges such as south-central Hikurangi is reproducible with a décollement strength based on friction measurements from laboratory experiments on weak clay minerals, and with an increase in frictional strength with temperature due to clay mineral transformations. The inner wedge may be stable or attain criticality only episodically as new material is incorporated into the wedge. The effective basal friction in the outer wedge is predicted to be low, increasing the probability that transient stress changes (e.g., from earthquake ruptures) may change the stress state there.

Acknowledgements

This work was supported by Marsden grant GNS1204 (Ellis, Ghisetti, Barnes), ERC Starting Grant 715836 (Fagereng), Direct Core Funding to GNS Science through the 'Tectonics of Zealandia' programme, and to NIWA through the Coasts and Oceans Centre programme Active Seafloor Processes and Resources. We thank many colleagues for previous discussions on this topic, including: Juli Morgan, Dan Barker, Stuart Henrys, Dan Bassett, Laura Wallace, Demian Saffer, Rob Harris, Charles Williams, James Biemiller, Heather Savage, Kelin Wang, and Tian Sun. We also acknowledge constructive reviews from two anonymous reviewers. In this paper, Ellis was lead author and wrote the bulk of the manuscript and performed the numerical analyses; Ghisetti and Barnes contributed text and figures to the sections on geological setting and transect ET2, and to the discussion; Boulton contributed to the section on frictional properties and the discussion; and Fagereng and Buiter contributed to the discussion about critical wedge theory and its application.

References

Antriasian, A., Harris, R.N., Tréhu, A.M., Henrys, S.A., Phrampus, B.J., Lauer, R., Gorman, A.R., Pecher, I.A. & Barker, D., 2019. Thermal regime of the Northern Hikurangi margin, New Zealand, *Geophys. J. Int.,* **216**, 1177-1190, doi:10.1093/gji/ggy450.

Ballance, P. F., 1976. Evolution of the upper Cenozoic magmatic arc and plate boundary in northern New Zealand, *Earth planet. Sci. Lett.,* **28**, 356-370, doi:10.1016/0012-821X(76)90197-7.

Barker, D.H., Sutherland, R., Henrys, S. & Bannister, S., 2009. Geometry of the Hikurangi subduction thrust and upper plate, North Island, New Zealand, *Geochem. Geophys. Geosyst.,* **10**, doi:10.1029/2008GC002153.

Barker, D. H., Henrys, S., Caratori Tontini, F., Barnes, P. M., Bassett, D., Todd, E. & Wallace, L., 2018. Geophysical constraints on the relationship between seamount subduction, slow slip and tremor at the north Hikurangi subduction zone, New Zealand, *Geophys. Res. Lett.,* **45**, 12804-12813, doi:10.1029/2018GL080259.

Barnes, P.M. & Mercier de Lépinay, B., 1997, Rates and mechanics of rapid frontal accretion along the very obliquely convergent southern Hikurangi margin, New Zealand, *J. geophys. Res.: Solid Earth,* **102**, 24931–24952, doi:10.1029/97JB01384.

Barnes, P.M., Lamarche, G., Bialas, J., Henrys, S., Pecher, I., Netzeband, G.L., Greinert, J., Mountjoy, J.J., Pedley, K. & Crutchley, G., 2010, Tectonic and geological framework for gas hydrates and cold seeps on the Hikurangi subduction margin, New Zealand, *Mar. Geol.,* **272**, 26–48, doi:10.1016/j.margeo.2009.03.012.

Barnes, P.M., Ghisetti, F.C., Ellis, S. & Morgan, J.K., 2018. The role of protothrusts in frontal accretion and accommodation of plate convergence, Hikurangi subduction margin, New Zealand, *Geosphere*, **14**, doi:10.1130/GES01552.1.

Bassett, D., Sutherland, R. & Henrys, S., 2014. Slow wavespeeds and fluid overpressure in a region of shallow geodetic locking and slow slip, Hikurangi subduction margin, New Zealand, *Earth planet. Sci. Lett.,* **389**, 1–13, doi:10.1016/j.epsl.2013.12.021.

Beall, A., Fagereng, Å. & Ellis, S.M., 2019. Strength of strained two-phase mixtures: application to rapid creep and stress amplification in subduction zone melange, *Geophys. Res. Lett.,* **46**, 169-178; doi:10.1029/2018GL081252.

Beavan, J., Tregoning, P., Bevis, M., Kato, T. & Meertens, C., 2002, Motion and rigidity of the Pacific Plate and implications for plate boundary deformation, *J. geophys. Res.: Solid Earth,* **107**, 2261, doi:10.1029/2001JB000282.

Behnsen, J. & Faulkner, D.R., 2012. The effect of mineralogy and effective normal stress on frictional strength of sheet silicates, *J. Struct. Geol.,* **42**, 49-61, doi:10.1016/j.jsg.2012.06.015.

Bell, R., Sutherland, R., Barker, D.H., Henrys, S., Bannister, S., Wallace, L. & Beavan, J., 2010. Seismic reflection character of the Hikurangi subduction interface, New Zealand, in the region of repeated Gisborne slow slip events, *Geophys. J. Int.,* **180**, 34–48, doi:10.1111/j.1365-246x.2009.04401.x.

Bell, R., Holden, C., Power, W., Wang, X. & Downes, G., 2014. Hikurangi margin tsunami earthquake generated by slow seismic rupture over a subducted seamount, *Earth planet. Sci. Lett.*, **397**, 1-9, doi:10.1016/j.epsl.2014.04.005.

Bland, K.J., Uruski, C.I. & Isaac, M.J., 2015, Pegasus Basin, eastern New Zealand: A stratigraphic record of subsidence and subduction, ancient and modern, *New Zeal. J. Geol. Geophys.,* **58**, 319–343, doi:10.1080/00288306.2015.1076862.

Bos, B. & Spiers, C.J., 2001. Experimental investigation into the microstructural and mechanical evolution of phyllosilicate-bearing fault rock under conditions favouring pressure solution*, J. Struct. Geol.,* **23**, 1187-2002, doi:10.1016/s0191-8141(00)00184-x.

Bos, B. & Spiers, C.J., 2002. Frictional-viscous flow of phyllosilicate-bearing fault rock: Microphysical model and implications for crustal strength profiles, *J. Geophys. Res.*, *Solid Earth,* **107**, 2028, doi:10.1029/2001JB000301.

Boulton, C., Niemeijer, A.R., Hollis, C.J., Townend, J., Raven, M., Kulhanek, D.K., & Shepherd, C.L., 2019. Temperature-dependent frictional properties of heterogeneous Hikurangi Subduction Zone input sediments, ODP Site 1124, *Tectonophys.*, in press, March 2019, doi:10.1016/j.tecto.2019.02.006.

Brown, K.M., Kopf, A., Underwood, M.B., Weinberger, & J.L., 2003. Compositional and fluid pressure controls on the state of stress on the Nankai subduction thrust: A weak plate boundary, *Earth Planet. Sci. Lett.*, **214**, 589-603, doi:10.1016/S0012-821X(03)00388-1.

Buiter, S.J.H., 2012. A review of brittle compressional wedge models, Tectonophys., **530–531**, 1-17, doi:10.1016/j.tecto.2011.12.018.

Buiter, S. & Ellis, S., 2012. SULEC: Benchmarking a new ALE finite-element code, *EGU General Assembly Conference Abstracts* **14**, EGU2012-7528.

Bullock, R.J., De Paola, N. & Holdsworth, R.E., 2015. An experimental investigation into the role of phyllosilicate content on earthquake propagation during seismic slip in carbonate faults, *J. geophys. Res.: Solid Earth,* **120**, 3187-3207, doi:10.1002/2015jb011914.

Burgreen-Chan, B., Meisling, K.E. & Graham, S., 2016. Basin and petroleum system modelling of the East Coast Basin, New Zealand: a test of overpressure scenarios in a convergent margin, *Basin Res.,* **28**, 536-567, doi:10.1111/bre.12121.

Carpenter, B. M., Scuderi, M. M., Collettini C. & Marone, C., 2014. Frictional heterogeneities on carbonate-bearing normal faults: Insights from the Monte Maggio Fault, Italy, *J. geophys. Res.: Solid Earth*, **119**, 9062–9076, doi:10.1002/2014JB011337.

Carter, R. M., McCave, I.N. & L. Carter, L., 2004. Leg 181 synthesis: fronts, flows, drifts, volcanoes, and the evolution of the southwestern gateway to the Pacific Ocean, eastern New Zealand, in *Proceedings of the Ocean Drilling Program, Scientific Results*, **181**, edited by C. Richter, 1-111, doi:10.2973/odp/proc.sr.181.210.2004.

Carter, R.M., McCave, I.N., Richter, C., Carter, L., et al., 1999. *Proc. ODP, Init. Repts.,* **181**, College Station, TX (Ocean Drilling Program), doi:10.2973/odp.proc.ir.181.2000.

Casey Moore, J., Klaus, A., Bangs, N.L., Bekins, B., Bücker, C.J., Brückmann, W., Erickson, S.N., Hansen, O., Horton, T., Ireland, P. & Major, C.O., 1998. Consolidation patterns during initiation and evolution of a plate-boundary décollement zone: Northern Barbados accretionary prism, *Geology*, **26**, 811-814, doi:10.1029/2002jb002314.

Chen, J., Verberne, B.A. & Spiers, C.J., 2015. Interseismic re-strengthening and stabilization of carbonate faults by "non-Dieterich" healing under hydrothermal conditions, *Earth Planet. Sci. Lett.*, **423**, 1-12, doi: 10.1016/j.epsl.2015.03.044.

Clark, K., Howarth, J., Litchfield, N., Cochran, U., Turnbull, J., Dowling, L., Howell, A., Berryman, K. & Wolfe, F., 2019. Geological evidence for past large earthquakes and tsunamis along the Hikurangi subduction margin, New Zealand, *Mar. Geol.*, 412, 139-172, doi:10.1016/j.margeo.2019.03.004.

Colletta, B., Letouzey, J., Pinedo, R., Ballard, J. F. & Balé, P., 1991. Computerized X-ray tomography analysis of sandbox models: Examples of thin-skinned thrust systems, *Geology*, **19**, 1063-1067, doi:10.1130/0091-7613(1991)019<1063:cxrtao>2.3.co;2.

Collettini, C., Niemeijer, A., Viti, C. & Marone, C., 2009. Fault zone fabric and fault weakness, *Nature*, **462**, 907-910, doi:10.1038/nature08585.

Colton-Bradley, V. A., 1987. Role of pressure in smectite dehydration—Effects on geopressure and smectite-to-illite transformation, *Am. Assoc. Pet. Geol. Bull.*, **71**, 1414-1427, doi:10.1306/703c8092-1707-11d7-8645000102c1865d.

Dahlen, F.A., 1984. Noncohesive critical Coulomb wedges: an exact solution, *J. geophys. Res.: Solid Earth,* **89**, 10125–10133, doi:10.1029/jb089ib12p10125.

Dahlen, F. A., 1990. Critical Taper Model of Fold-And-Thrust Belts and Accretionary Wedges, *Ann. Rev. Earth Planet. Sci.,***18**, 55-99, doi:10.1146/annurev.earth.18.1.55.

Darby, D. & Funnell, R.H., 2001. Overpressure associated with a convergent plate margin: East Coast Basin, *New Zeal. Petrol. Geosci.*, **7**, 291-299, doi:10.1144/petgeo.7.3.291.

Davis, D., Suppe, J. & Dahlen, F.A., 1983. Mechanics of fold-and-thrust belts and accretionary wedges, *J. geophys. Res.: Solid Earth (1978–2012),* **88**, 1153–1172, doi: 10.1029/JB088iB02p01153.

Davy B.W. & Wood, R., 1994. Gravity and magnetic modelling of the Hikurangi Plateau, *Mar. Geol.,* **118**, 139-152, doi:10.1016/0025-3227(94)90117-1.

Davy, B.R., Hoernle, K. & Werner, R., 2008. The Hikurangi Plateau—Crustal structure, rifted formation and Gondwana subduction history, *Geochem. Geophys. Geosyst.* **9**, Q07004, doi:10.1029/2007GC001855.

DeMets, C., Gordon, R. G., Argus, D. F. & Stein, S., 1994. Effect of recent revisions to the geomagnetic reversal time scale on estimates of current plate motions, *Geophys. Res. Lett.,* **21**, 2191-2194, doi:10.1029/94gl02118.

den Hartog, S. A. M.; Spiers, C. J., 2013. Influence of subduction zone conditions and gouge composition on frictional slip stability of megathrust faults, *Tectonophys*., **600**, 75-90, doi: 10.1016/j.tecto.2012.11.006

Dominguez, S., Malavieille, J. & Lallemand, S. E., 2000. Deformation of accretionary wedges in response to seamount subduction: Insights from sandbox experiments, *Tectonics*, **19**, 182-196, doi:10.1029/1999tc900055.

Eberhart-Phillips, D., Reyners, M., Chadwick, M. & Chiu, J.M., 2005. Crustal heterogeneity and subduction processes: 3-D Vp, Vp/Vs and Q in the southern North Island, New Zealand, *Geophys. J. Int.,* **162**, 270–288, doi:10.1111/j.1365-246x.2005.02530.x.

Eberhart-Phillips, D., Reyners, M., Chadwick, M. & Stuart, G., 2008. Three dimensional attenuation structure of the Hikurangi subduction zone in the central North Island, New Zealand, *Geophys. J. Int.,* **174**, 418–434, doi:10.1111/j.1365-246x.2008.03816.x.

Eberhart-Phillips, D. & Bannister, S., 2015. 3-D imaging of the northern Hikurangi subduction zone, New Zealand: variations in subducted sediment, slab fluids and slow slip, *Geophys. J. Int.,* **201**, 838-855, doi:10.1093/gji/ggv057.

Eberhart-Phillips, D., Bannister, S. & Reyners, M., 2017. Deciphering the 3-D distribution of fluid along the shallow Hikurangi subduction zone using P-and S-wave attenuation. *Geophys. J. Int.*, **211**, 1032-1045, doi: 10.1093/gji/ggx348.

Ellis, S., Pecher, I., Kukowski, N., Xu, W., Henrys, S. & Greinert, J., 2010. Testing proposed mechanisms for seafloor weakening at the top of gas hydrate stability on an uplifted submarine ridge (Rock Garden), New Zealand, *Mar. Geol.,* **272**,127-140, doi:10.1016/j.margeo.2009.10.008.

Ellis, S.M., Little, T.A., Wallace, L.M., Hacker, B.R. & Buiter, S.J.H., 2011. Feedback between rifting and diapirism can exhume ultrahigh-pressure rocks, *Earth planet. Sci. Lett.,* **311**, 427-438, doi:10.1016/j.epsl.2011.09.031.

Ellis S., Fagereng Å., Barker D., Henrys S., Saffer D., Wallace L., Williams C. & Harris R., 2015. Fluid budgets along the northern Hikurangi subduction margin, New Zealand: the effect of a subducting seamount on fluid pressure, *Geophys. J. Int.,* **202**, 277–297, doi:10.1093/gji/ggv127.

England, P., 2018. On shear stresses, temperatures, and the maximum magnitudes of earthquakes at convergent plate boundaries, *J. geophys. Res.: Solid Earth,* **123**, 7165-7202, doi:10.1029/2018JB015907.

Fagereng, Å., 2011. Wedge geometry, mechanical strength, and interseismic coupling of the Hikurangi subduction thrust, New Zealand, *Tectonophys*, **507**(1-4), 26-30, doi:10.1016/j.tecto.2011.05.004.

Fagereng, Å. & Ellis, S., 2009. On factors controlling the depth of interseismic coupling on the Hikurangi subduction interface, New Zealand, *Earth planet. Sci. Lett.,* **278**, 120–130, doi:10.1016/j.epsl.2008.11.033.

Fagereng, Å. & Sibson, R.H., 2010. Mélange rheology and seismic style, *Geology*, **38**, 751-754, doi:10.1130/g30868.1.

Fagereng, Å. & den Hartog, S.A.M., 2017. Subduction megathrust creep governed by pressure solution and frictional-viscous flow, *Nat. Geosci.,* **10**, doi:10.1038/ngeo2857.

Fagereng, Å., Diener, J.F.A., Ellis, S. & Remitti, F., 2018. Fluid-related deformation processes at the up- and down-dip limits of the subduction thrust seismogenic zone: What do the rocks tell us? in Byrne, T., Fisher, D., McNeill, L., Saffer, D., Ujiie, K., Underwood, M., and Yamaguchi, A., eds., Geology and Tectonics of Subduction Zones: A Tribute to Gaku Kimura, *Geol. Soc. Am. Spec. Pap.,* **534**, 1–30, doi: 10.1130/2018.2534.

Faulkner, D.R., Mitchell, T.M., Behnsen, J., Hirose, T. & Shimamoto, T., 2011. Stuck in the mud? Earthquake nucleation and propagation through accretionary forearcs, *Geophys. Res. Lett.,* **38**, L18303, doi:10.1029/2011GL048552.

Field, B. D., Uruski, C.I., Beu, A., et. al., 1997. Cretaceous-Cenozoic geology and petroleum systems of the East Coast Region, *Institute of Geological and Nuclear Sciences monograph* **19**, 301 pp., Institute of Geological and Nuclear Sciences Limited, Lower Hutt.

Freed, R.L. & Peacor, D.R., 1989. Variability in temperature of the smectite/illite reaction in Gulf Coast sediments, *Clay Minerals*, **24**, 171–180, doi:10.1180/claymin.1989.024.2.05.

Fullsack, P., 1995. An arbitrary Lagrangian-Eulerian formulation for creeping flows and its application in tectonic models, *Geophys. J. Int.*, **120**, 1-23, doi:10.1111/j.1365-246x.1995.tb05908.x.

Ghisetti, F.C., Barnes, P.M., Ellis, S., Plaza-Faverola, A. & Barker, D.H.N., 2016. The last 2 Myr of accretionary wedge construction in the central Hikurangi margin (North Island,

New Zealand): Insights from structural modelling, *Geochem. Geophys. Geosyst.,* **17**, 2661–2686, doi:10 .1002/2016GC006341.

Greinert, J., Lewis, K., Bialas, J., Pecher, I., Rowden, A., Bowden, D., De Batis, M. & Linke, P., 2010. Methane seepage along the Hikurangi Margin, New Zealand: Overview of studies in 2006 and 2007 and new evidence from visual, bathymetric and hydroacoustic investigations, *Mar. Geol.,* **272**, 6–25, doi:10.1016/j.margeo.2010.01 .017.

Ikari, M. J., Saffer, D.M. & Marone, C., 2009a. Frictional and hydrologic properties of clay-rich gouge, *J. geophys. Res.: Solid Earth (1978–2012)*, **114**, B05409, doi:10.1029/2008JB006089.

Ikari, M. J., Saffer, D.M. & Marone, C., 2009b. Frictional and hydrologic properties of a major splay fault system, Nankai subduction zone, *Geophys. Res. Lett.,* **36**, L20313, doi:10.1029/2009GL040009.

Ikari, M. J., Hüpers, A. & Kopf, A. J., 2013a. Shear strength of sediments approaching subduction in the Nankai Trough, Japan as constraints on forearc mechanics, *Geochem. Geophys. Geosyst.*, **14**, 2716-2730, doi:10.1002/ggge.20156.

Ikari, M.J., Niemeijer, A.R., Spiers, C.J., Kopf, A.J. & Saffer, D.M., 2013b. Experimental evidence linking slip instability with seafloor lithology and topography at the Costa Rica convergent margin, *Geology*, **41**, 891-894, doi:10.1130/g33956.1.

Ikari, M.J., Y. Ito, K. Ujiie & Kopf, A.J., 2015. Spectrum of slip behavior in Tohoku fault zone samples at plate tectonic slip rates, *Nat. Geosci.,* **8**, doi:10.1038/NGEO2547.

Jefferies, S. P., Holdsworth, R. E., Shimamoto, T., Takagi, H., Lloyd, G. E. & Spiers, C. J., 2006. Origin and mechanical significance of foliated cataclastic rocks in the cores of

crustal-scale faults: Examples from the Median Tectonic Line, Japan, *J. geophys. Res.: Solid Earth (1978–2012),* **111**, B12303, doi:10.1029/2005jb004205.

Kano, M., Fukuda, J.I., Miyazaki, S.I. & Nakamura, M., 2018. Spatiotemporal evolution of recurrent slow slip events along the southern Ryukyu subduction zone, Japan, from 2010 to 2013, *J. geophys. Res.: Solid Earth*, **123**, 7090-7107, doi:10.1029/2018JB016072.

Kimura, G., Kitamura, Y., Hashimoto, Y., Yamaguchi, A., Shibata, T., Ujiie, K. & Okamoto, S.Y., 2007. Transition of accretionary wedge structures around the up-dip limit of the seismogenic subduction zone, *Earth planet. Sci. Lett.*, **255**, 471-484, doi:10.1016/j.epsl.2007.01.005.

Kodaira S., Iidaka T., Kato A., Park J.-O., Iwasaki T. & Kaneda Y., 2004. High Pore Fluid Pressure May Cause Silent Slip in the Nankai Trough, *Science*, **304**, 1295-1298, doi:10.1126/science.1096535.

Kopp, H. & Kukowski, N., 2003. Backstop geometry and accretionary mechanics of the Sunda margin, *Tectonics*, **22**, doi: 10.1029/2002TC001420.

Koyi, H.A. & Vendeville, B.C., 2003. The effect of décollement dip on geometry and kinematics of model accretionary wedges, *J. Struct. Geol.,* **25**, 1445–1450, doi:10.1016/s0191-8141(02)00202-x.

Lauer, R.M. & Saffer, D.M., 2012. Fluid budgets of subduction zone forearcs: the contribution of splay faults. *Geophys. Res. Lett.,* **39**, doi:10.1029/2012GL052182.

Lauer, R.M., Saffer, D.M. & Harris, R.N., 2017. Links between clay transformation and earthquakes along the Costa Rican subduction margin, *Geophys. Res. Lett.,* **44**, 7725-7732, doi:10.1002/2017GL073744.

Lee, J.M. & Begg, J.G., 2002. Geology of the Wairarapa area: scale 1:250,000. Lower Hutt: Institute of Geological & Nuclear Sciences Limited. *Institute of Geological & Nuclear Sciences 1:250,000 geological map,* **11**, 66 p. + 1 fold map.

Lempp, C., Witthaus, M., Roeckel, T., Hecht, K. & Herold, M., 2010. Geomechanisches Verhalten diagenetisch unterschiedlich stark verfestigter pelitischer Gesteine in tiefen Geothermiebohrungen, *Zeitschrift der Deutschen Gesellschaft für Geowissenschaften,* **161**, 379–400, doi:10.1127/1860-1804/2010/0161-0379.

Lewis, K. B. & Pettinga, J. R., 1993. The emerging, imbricate frontal wedge of the Hikurangi Margin, *In:* Ballance, P. F. ed. South Pacific sedimentary basins. *Sedimentary basins of the world 2.* Amsterdam, Elsevier. pp. 225-250.

Lewis, K.B., Collot, J.Y. & Lallem, S.E., 1998. The dammed Hikurangi Trough: a channel-fed trench blocked by subducting seamounts and their wake avalanches (New Zealand–France GeodyNZ Project), *Basin Res.*, **10**, 441–468, doi:10.1046/j.1365-2117.1998.00080.x.

Lewis, K.B. & Pantin, H.M., 2002. Channel-axis, overbank and drift sediment waves in the southern Hikurangi Trough, New Zealand, *Mar. Geol.,* **192**, 123–151, doi:10.1016 /S0025 -3227(02)00552-2.

Lohrmann, J., Kukowski, N., Adam, J. & Oncken, O., 2003. The impact of analogue material properties on the geometry, kinematics, and dynamics of convergent sand wedges, *J. Struct. Geol.,* **25**, 1691–1711, doi:10.1016/s0191-8141(03)00005-1.

Logan, J.M. & Rauenzahn, K.A., 1987. Frictional dependence of gouge mixtures of quartz and montmorillonite on velocity, composition and fabric, *Tectonophys.*, **144**, 87-108, doi:10.1016/0040-1951(87)90010-2.

Moore, P.R., 1988. Stratigraphy, composition and environment of deposition of the Whangai Formation and associated Late Cretaceous-Paleocene rocks, eastern North Island, New Zealand, *New Zeal. Geol. Survey Bull.,* **100**, 1-82.

Moore, D.E. & Lockner, D.A., 2007. Friction of the smectite clay montmorillonite: A review and interpretation of data, in *The Seismogenic Zone of Subduction Thrust Faults*, edited by T. Dixon and C. Moore, pp. 317-345, Columbia Univ. Press, New York, doi:10.7312/dixo13866-011.

Moore, J.C. & Byrne, T., 1987. Thickening of fault zones: A mechanism of melange formation in accreting sediments, *Geology*, **15**, 1040-1043, doi:10.1130/0091-7613(1987)15<1040:tofzam>2.0.co;2.

Moore, G.F., Shipley, T.H., Stoffa, P.L., Karig, D.E., Taira, A., Kuramoto, S., Tokuyama, H. & Suyehiro, K., 1990. Structure of the Nankai Trough accretionary zone from multichannel seismic reflection data, *J. geophys. Res.: Solid Earth (1978–2012),* **95**, 8753–8765, doi:10 .1029 /JB095iB06p08753.

Moore, J.C. & Saffer, D., 2001. Updip limit of the seismogenic zone beneath the accretionary prism of southwest Japan: An effect of diagenetic to low-grade metamorphic processes and increasing effective stress, *Geology*, **29**, 183-186, doi: 10.1130/00917613(2001)029<0183:ulotsz>2.0.co;2.

Moore, J.C., Rowe, C. & Meneghini, F., 2007. How Accretionary Prisms Elucidate Seismogenesis in Subduction Zones, *The Seismogenic Zone of Subduction Thrust Faults*, p. 288, doi:10.7312/dixo13866-010.

Morgan, J.K. & Bangs, N.L., 2017. Recognizing seamount-forearc collisions at accretionary margins: Insights from discrete numerical simulations, *Geology*, **47**, 635-638, doi:10.1130/g38923.1.

Morgans, H.E.G, Crundwell, M.P., Scott, G.H & Edwards, A.R., 1995. Biostratigraphy of Titihaoa-1 offshore petroleum exploration well, Wairarapa Coast, New Zealand, *Institute of Geological and Nuclear Sciences client report*, 53492A.10.

Morrow, C. A., Moore, D. E. & Lockner, D. A., 2017. Frictional strength of wet and dry montmorillonite, *J. geophys. Res.: Solid Earth*, **122**, 3392-3409, doi:10.1002/2016JB013658.

Mortimer, N. & Parkinson, D.L., 1996. Hikurangi Plateau: a Cretaceous large igneous province in the southwest Pacific Ocean, *J. geophys. Res.: Solid Earth (1978–2012)*, **101**, 687-696, doi:10.1029/95jb03037.

Mountjoy, J.J. & Barnes, P.M., 2011. Active upper plate thrust faulting in regions of low plate interface coupling, repeated slow slip events, and coastal uplift: Example from the Hikurangi Margin, New Zealand, *Geochem. Geophys. Geosyst.*, **12**, Q01005, doi:10.1029/2010GC003326.

Niemeijer, A., Marone, C. & Elsworth, D., 2010. Fabric induced weakness of tectonic faults, *Geophys. Res. Lett.,* **37**, L03304, doi:10.1029/2009GL041689.

Nicol, A. & Wallace, L. M. 2007. Temporal stability of deformation rates: Comparison of geological and geodetic observations, Hikurangi subduction margin, New Zealand, *Earth planet. Sci. Lett.,* **258**, 397-413, doi:10.1016/j.epsl.2007.03.039.

Park, J.O., Tsuru, T., Takahashi, N., Hori, T., Kodaira, S., Nakanishi, A., Miura, S. & Kaneda, Y., 2002. A deep strong reflector in the Nankai accretionary wedge from multichannel seismic data: Implications for underplating and interseismic shear stress release, *J. geophys. Res.: Solid Earth (1978–2012),* **107**, 2061-2077, doi:10.1029/2001jb000262.

Pecher, I.A. et al., 2010. Focussed fluid flow on the Hikurangi Margin, New Zealand—evidence from possible local upwarping of the base of gas hydrate stability, *Mar. Geol.,* **272**, 99–113, doi:10.1016/j.margeo.2009.10.006.

Pedley, K.L., Barnes, P.M., Pettinga, J.R. & Lewis, K.B., 2010. Seafloor structural geomorphic evolution of the accretionary frontal wedge in response to seamount subduction, Poverty Indentation, New Zealand, *Mar. Geol.,* **270**, 119–138, doi:10.1016/j.margeo.2009.11.006.

Pelletier, D., Fortin, A. & Camarero, R., 1989. Are FEM solutions of incompressible flows really incompressible? (or how simple flows can cause headaches!), *Int. J. Num. Meth. Fluids,* **9**, 99-112, doi:10.1002/fld.1650090108.

Peltonen, C., Marcussen, Ø., Bjørlykke, K. & Jahren, J., 2009. Clay mineral diagenesis and quartz cementation in mudstones: The effects of smectite to illite reaction on rock properties, *Mar. Petrol. Geol.,* **26**, 887-898, doi:10.1016/j.marpetgeo.2008.01.021.

Pettinga, J. R., 1982. Upper Cenozoic structural history, coastal southern Hawke's Bay, New Zealand, *New Zeal. J. Geol. Geophys.,* **25**, 149-191, doi:10.1080/00288306.1982.10421407.

Plaza-Faverola, A., Klaeschen, D., Barnes, P.M., Pecher, I., Henrys, S. & Mountjoy, J., 2012. Evolution of fluid explusion and concentrated hydrate zones across the southern Hikurangi subduction margin, New Zealand: An analysis from depth migrated seismic data, *Geochem. Geophys. Geosyst.,* **13**, Q08019, doi:10.1029/2012GC004228.

Plaza-Faverola, A., Pecher, I., Crutchley, G., Barnes, P.M., Bünz, S., Golding, T., Klaeschen, D., Papenberg, C. & Bialas, J., 2014. Submarine gas seepage in a mixed contractional and shear deformation regime: Cases from the Hikurangi oblique-subduction margin, *Geochem. Geophys. Geosyst.,* **15**, 416–433, doi:10 .1002 /2013GC005082.

Plaza-Faverola, A., Henrys, S., Pecher, I., Wallace, L. & Klaeschen, D., 2016. Splay fault branching from the Hikurangi subduction shear zone: Implications for slow slip and fluid flow, *Geochem. Geophys. Geosyst.*, **17**, 5009–5023, doi:10 .1002/2016GC006563.

Power, W., Wallace, L.M., Mueller, C., Henrys, S., Clark, K., Fry, B., Wang, X. & Williams, C., 2016. Understanding the potential for tsunami generated by earthquakes on the

southern Hikurangi subduction interface, *New Zeal. J. Geol. Geophys.* **59**, 70-85, doi: 10.1080/00288306.2015.1127825.

Quinquis, M.E., Buiter, S.J. & Ellis, S., 2011. The role of boundary conditions in numerical models of subduction zone dynamics, *Tectonophys.*, **497**, 57-70, doi:10.1016/j.tecto.2010.11.001.

Rabinowitz, H.S., Savage, H.M., Skarbek, R.M., Ikari, M.J., Carpenter, B.M. & Collettini, C., 2018. Frictional Behavior of Input Sediments to the Hikurangi Trench, New Zealand, *Geochem. Geophys. Geosyst.,* **19**, 2973-2990, doi:10.1029/2018GC007633.

Reyes, A., Christenson, B. & Faure, K., 2010. Sources of solutes and heat in low-enthalpy mineral waters and their relation to tectonic setting, *New Zealand, J. Volc. Geotherm. Res.,* **192**, 117–141.

Reyners,M., Eberhart-Phillips, D., Stuart, G. & Nishimura, Y., 2006. Imaging subduction from the trench to 300 km depth beneath the central North Island, New Zealand, with Vp and Vp/Vs, *Geophys. J. Int.,* **165**, 565–583, doi:10.1111/j.1365-246x.2006.02897.x.

Rijsingen, E., Lallemand, S., Peyret, M., Arcay, D., Heuret, A., Funiciello, F. & Corbi, F. (2018). How subduction interface roughness influences the occurrence of large interplate earthquakes. *Geochem., Geophys., Geosys.*, **19**, 2342– 2370, doi:10.1029/2018GC007618.

Rowe, C. D., Casey Moore, J., Remitti, F. & IODP Expedition 343/343T Scientists, 2013. The thickness of subduction plate boundary faults from the seafloor into the seismogenic zone, *Geology*, **41**, 991-994, doi:10.1130/g34556.1.

Saffer, D.M. &. Wallace, L.M., 2015. The frictional, hydrologic, metamorphic and thermal habitat of shallow slow earthquakes, *Nat. Geosci.,* **8**, doi:10.1038/ngeo2490.

Saffer, D. M. & Marone, C., 2003. Comparison of smectite-and illite-rich gouge frictional properties: application to the updip limit of the seismogenic zone along subduction megathrusts, *Earth planet. Sci. Lett.*, **215**, 219-235, doi:10.1016/s0012-821x(03)00424-2.

Saffer, D. M., Lockner, D. A. & McKiernan, A., 2012. Effects of smectite to illite transformation on the frictional strength and sliding stability of intact marine mudstones, *Geophys. Res. Lett.,* **39**, L11304, doi:10.1029/2012GL051761.

Scholz, C.H., 1998. Earthquakes and friction laws, *Nature*, **391**, 37-42, doi:10.1038/34097.

Schreurs, G., Buiter, S.J.H., Boutelier, D., Corti, G., Costa, E., Cruden, A.R., Daniel, J.-M., Hoth, S., Koyi, H.A., Kukowski, N., Lohrmann, J., Ravaglia, A., Schlische, R.W., Withjack, M.O., Yamada, Y., Cavozzi, C., Delventisette, C., Elder Brady, J.A., Hoffmann-Rothe, A., Mengus, J.-M., Montanari, D. & Nilforoushan, F., 2006. Analogue benchmarks of shortening and extension experiments. In: Buiter, S.J.H., Schreurs, G. (Eds.), Analogue and numerical modelling of crustal-scale processes, *Geol. Soc. London Spec. Publ*., **253**, 1–27, doi:10.1144/gsl.sp.2006.253.01.01.

Schumann, K., Behrmann, J.H., Stipp, M., Yamamoto, Y., Kitamura, Y. & Lempp, C., 2014. Geotechnical behavior of mudstones from the Shimanto and Boso accretionary complexes, and implications for the Nankai accretionary prism, *Earth, Plan. Space*, **66**, 129, doi:10.1186/1880-5981-66-129.

Sclater, J. G. & Christie, P. A. F., 1980. Continental stretching. an explanation of the post mid Cretaceous subsidence of the central North Sea, *J. geophys. Res.: Solid Earth (1978–2012),* **85**, 3711-3739, doi:10.1029/jb085ib07p03711.

Shaddox, H.R. & Schwartz, S.Y., 2019. Subducted seamount diverts shallow slow slip to the forearc of the northern Hikurangi subduction zone, New Zealand, *Geology,* doi:10.1130/G45810.1.

Shreve, R.L. & Cloos, M., 1986. Dynamics of sediment subduction, melange formation, and prism accretion, *J. geophys. Res.: Solid Earth (1978–2012),* **91**, 10229-10245, doi:10.1029/jb091ib10p10229.

Skarbek, R. M. & Rempel, A. W., 2017. Heterogeneous Coulomb wedges: Influence of fluid pressure, porosity, and application to the Hikurangi subduction margin, New Zealand, *J. geophys. Res.: Solid Earth*, **122**, 1585-1613, doi:10.1002/2016jb013497.

Smit, J.H.W., Brun, J.P. & Sokoutis, D., 2003. Deformation of brittle–ductile thrust wedges in experiments and nature, *J. geophys. Res.: Solid Earth (1978–2012),* **108**, doi:10.1029/2002JB002190.

Stirling, M., McVerry, G., Gerstenberger, M., Litchfield, N., Van Dissen, R., Berryman, K., Barnes, P., Wallace, L., Villamor, P., Langridge, R. & Lamarche, G., 2012. National seismic hazard model for New Zealand: 2010 update, *Bull. Seismol. Soc. Am.,* **102**, 1514-1542, doi:10.1785/0120110170.

Storti F. & McClay K., 1995. Influence of syntectonic sedimentation on thrust wedges in analogue models, *Geology*, **23**, 999–1002. doi:10.1130/0091-7613.

Tembe, S., Lockner, D.A. & T.-F. Wong, 2010. Effect of clay content and mineralogy on frictional sliding behaviour of simulated gouges: Binary and ternary mixtures of quartz, illite, and montmorillonite, *J. geophys. Res.: Solid Earth (1978–2012),***115**, B03416, doi:10.1029/2009jb006383.

Tesei, T., Collettini, C., Barchi, M.R., Carpenter, B.M. & Di Stefano, G., 2014. Heterogeneous strength and fault zone complexity of carbonate-bearing thrusts with possible implications for seismicity, *Earth planet. Sci. Lett.,* **408**, 307-318, doi:10.1016/j.epsl.2014.10.02.

Todd, E.K., Schwartz, S.Y., Mochizuki, K., Wallace, L.M., Sheehan, A.F., Webb, S.C., Williams, C.A., Nakai, J., Yarce, J., Fry, B. & Henrys, S., 2018. Earthquakes and Tremor Linked to Seamount Subduction During Shallow Slow Slip at the Hikurangi Margin, New Zealand, *J. geophys. Res.: Solid Earth,* **123**, 6769-6783, doi:10.1029/2018jb016136.

Trütner, S., Hüpers, A., Ikari, M.J., Yamaguchi, A., & Kopf, A.J., 2015. Lithification facilitates frictional instability in argillaceous subduction zone sediments, *Tectonophys.,* **665**, 177-185, doi:10.1016/j.tecto.2015.10.004.

Ujiie, K., Tanaks, H., Saito, T., et al., 2013. Low coseismic shear stress on the Tohoku-Oki megathrust determined from laboratory experiments, *Science*, **342**, 1211-1214, doi:10.1126/science.1243485.

Verberne, B.A.M, Spiers, C.J., Niemeijer, A.R., De Bresser, J.H.P, De Winter, D.A.M. & Plümper, O., 2014. Frictional properties and microstructure of calcite-rich fault gouges

sheared at sub-seismic sliding velocities, Pure Appl. Geophys., 171, 2617-2640, doi:10.1007/s00024-013-0760-0.

Verberne, B.A., Niemeijer, A.R., De Bresser, J.H.P. & Spiers, C.J., 2015. Mechanical behavior and microstructure of simulated calcite fault gouge sheared at 20–600°C: Implications for natural faults in limestones,,*J. geophys. Res.: Solid Earth*, **120**, 8169–8196, doi:10.1002/2015JB012292.

Von Huene, R. & Klaeschen, D., 1999. Opposing gradients of permanent strain in the aseismic zone and elastic strain across the seismogenic zone of the Kodiak shelf and slope, Alaska, *Tectonics*, **18**, 248–262, doi:10.1029/1998TC900022.

Vrolijk, P, 1990. On the mechanical role of smectite in subduction zones, *Geology*, **18**, 703–707, doi:10.1130/0091-7613(1990)018<0703:OTMROS>2.3.CO;2

Wallace, L. M., Beavan, J., McCaffrey, R. & Darby, D., 2004. Subduction zone coupling and tectonic block rotations in the North Island, New Zealand, *J. geophys. Res.: Solid Earth (1978–2012),***109**, doi:10.1029/2004JB003241.

Wallace, L.M. et al., 2009. Characterizing the seismogenic zone of a major plate boundary subduction thrust: Hikurangi Margin, New Zealand, *Geochem. Geophys. Geosyst.,* **10**, doi:10.1029/2009GC002610.

Wallace, L. M. & Beavan, J., 2010. Diverse slow slip behavior at the Hikurangi subduction margin, New Zealand, *J. geophys. Res.: Solid Earth (1978–2012)*, **115**, doi:10.1029/2010JB007717.

Wallace, L. M., Beavan, J., Bannister, S. & Williams, C., 2012. Simultaneous long-term and short-term slow slip events at the Hikurangi subduction margin, New Zealand:

Implications for processes that control slow slip event occurrence, duration, and migration, *J. geophys. Res.: Solid Earth (1978–2012)*, **117**, doi:10.1029/2012JB009489.

Wallace, L.M., Webb, S.C., Ito, Y., Mochizuki, K., Hino, R., Henrys, S., Schwartz, S.Y. & Sheehan, A.F., 2016. Slow slip near the trench at the Hikurangi subduction zone, New Zealand, *Science*, **352**, 701-704, doi:10.1126/science.aaf2349.

Wallace, L.M., Saffer, D.M., Barnes, P.M., Pecher, I.A., Petronotis, K.E., LeVay, L.J., and the Expedition 372/375 Scientists (2019). Hikurangi Subduction Margin Coring, Logging, and Observatories. Proceedings of the International Ocean Discovery Program, 372B/375: College Station, TX (International Ocean Discovery Program). doi.org/10.14379/iodp.proc.372B375.2019.

Wang, K. & Hu, Y., 2006. Accretionary prisms in subduction earthquake cycles: The theory of dynamic Coulomb wedge, *J. geophys. Res.: Solid Earth (1978–2012)*, **111**, B06410, doi:10.1029/2005JB004094.

Wang, K., Brown, L., Hu, Y., Yoshida, K., He, J. & Sun, T., 2019. Stable forearc stressed by a weak megathrust: Mechanical and geodynamic implications for stress changes caused by the M=9 Tohoku-oki earthquake, *J. Geophys. Res*., doi: 10.1029/2018JB017043

Webber, S., Ellis, S.M. & Fagereng, Å., 2018. "Virtual shear box" experiments of stress and slip cycling within a subduction interface mélange, *Earth Planet. Sci. Lett.,* **488**, 27-35, doi:10.1016/j.epsl.2018.01.035.

Wood, R. & Davy, B., 1994. The Hikurangi Plateau, *Mar. Geol.,* **118**, 153-173, doi:10.1016/0025-3227(94)90118-x.

Yamada, Y., Baba, K. & Matsuoka, T., 2006. Analogue and numerical modelling of accretionary prisms with a décollement in sediments, *Geol. Soc. Lond. Spec. Pub.,* **253**, 169–183, doi:10.1144/gsl.sp.2006.253.01.09.

Zhao, W.-L., Davis, D.M., Dahlen, F.A. & Suppe, J., 1986. Origin of convex accretionary wedges: evidence from Barbados, *J. geophys. Res.: Solid Earth (1978–2012)*, **91**, 10246–10258, doi:10.1029/jb091ib10p10246.

Figures

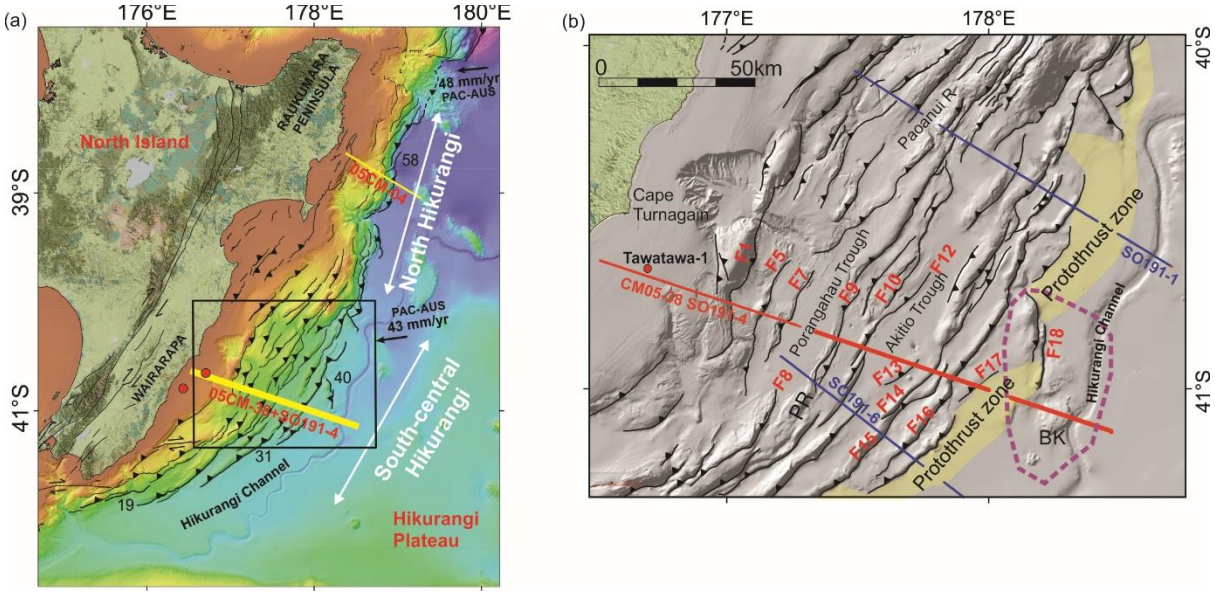

Figure 1. (a) Tectonic setting of the Pacific-Australia subduction zone and the North Island of New Zealand (Figure modified from Ghisetti et al., 2016) showing shaded bathymetry, northern and south-central Hikurangi margin and offshore thrust faults of the modern accretionary wedge. Short black arrows are the vectors of relative motion between the Pacific and Australian plates (DeMets et al., 1994; Beavan et al., 2002) while black numerals show trench convergence rates in mm/yr (Wallace et al., 2004). Box indicates area shown in (b). Red dots locate the Tawatawa-1 and Titihaoa-1 exploratory wells, respectively to the north and south (Field et al., 1997; Morgans et al., 1995). Thick yellow line shows the joined trace of the seismic reflection lines 05CM-38 and SO191-4 (Barnes et al., 2010; Ghisetti et al., 2016; Plaza-Faverola et al., 2016); location of northern line 05CM-04 (Barker et al., 2009) is also shown (thinner yellow line). (b) Closeup of study area. Red line shows the joined trace of the seismic reflection lines 05CM38 and SO191-4 (herein called "extended transect 2" (ET2)) (Ghisetti et al., 2016; Plaza-Faverola et al., 2016). Blue lines are the traces of neighbouring seismic reflection lines SO191-1 and SO191-6. Red dot shows Tawatawa-1 well. The approximate extent of Bennett Knoll seamount (BK) is shown with purple dashed line, and the protothrust zone is shown with yellow shading (Barnes et al., 2018). PR= Pōrangahau Ridge. Numbers F1-F18 refer to numbered thrust faults as defined by Ghisetti et al. (2016) and discussed in the text.

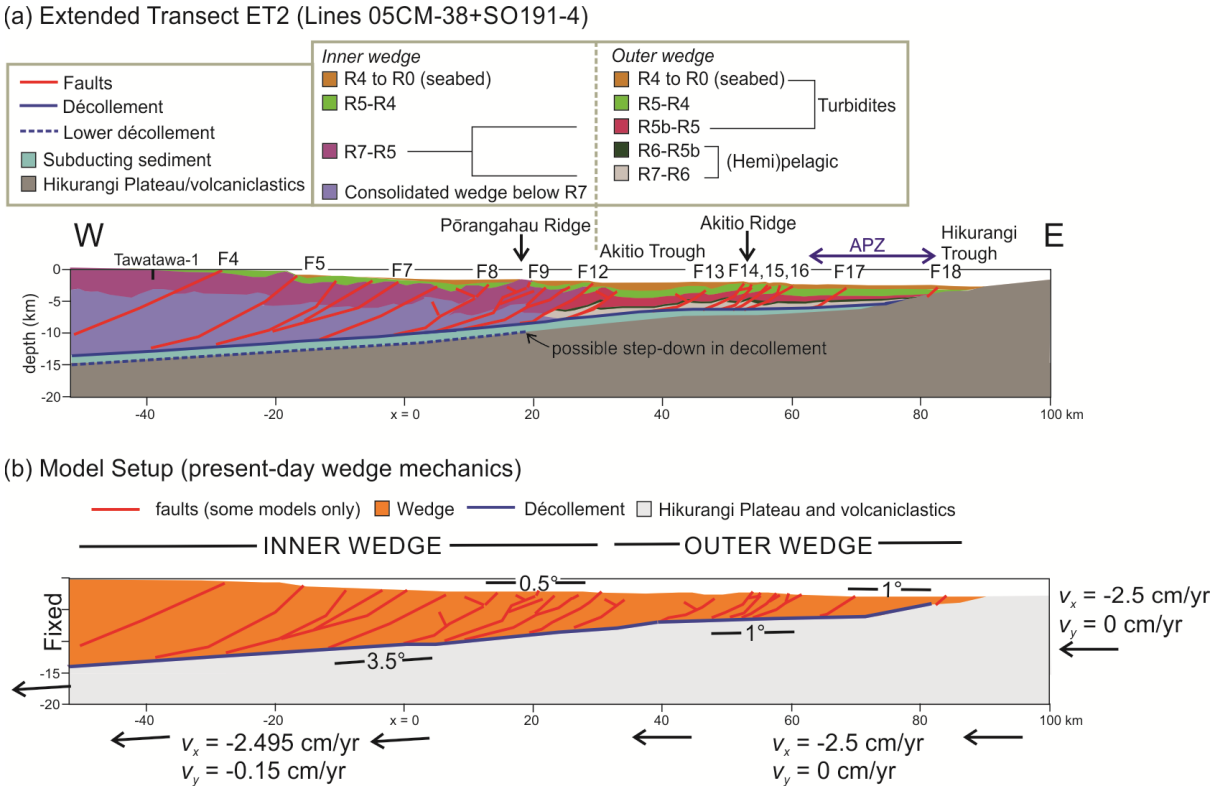

Figure 2. (a) Summary of the material properties and geometry of the present-day section ET2 on which the forward numerical model is based. The stack of imbricated units separated by prominent reflectors (R7, R6, R5b, R5, R4, R0) and the position of faults are based on the interpretation of seismic lines 05CM-38 and SO191-4 from Barnes et al. (2010); Ghisetti et al. (2016); Plaza Faverola et al. (2016) and Barnes et al. (2018). For the age of units bounded by reflectors R7 to R0 refer to Supplementary Note 1 and to Ghisetti et al. (2016). Dashed blue line = possible step-down in décollement investigated model P5 described later. APZ = Active Prototthrust Zone from Barnes et al. (2018). (b) Simplified model setup where all wedge material is represented by one material property (orange). Either one or two different friction coefficients are assigned to the décollement for the inner vs. outer wedge (blue). Subducted sediment and lower plate are coloured grey. Black arrows indicate velocity boundary conditions (subducting plate) relative to a fixed backstop (upper part of left-hand boundary). The different taper between inner and outer wedges is labelled. x = 0 marks the western-most location of the restored Transect 2 from Ghisetti et al. (2016).

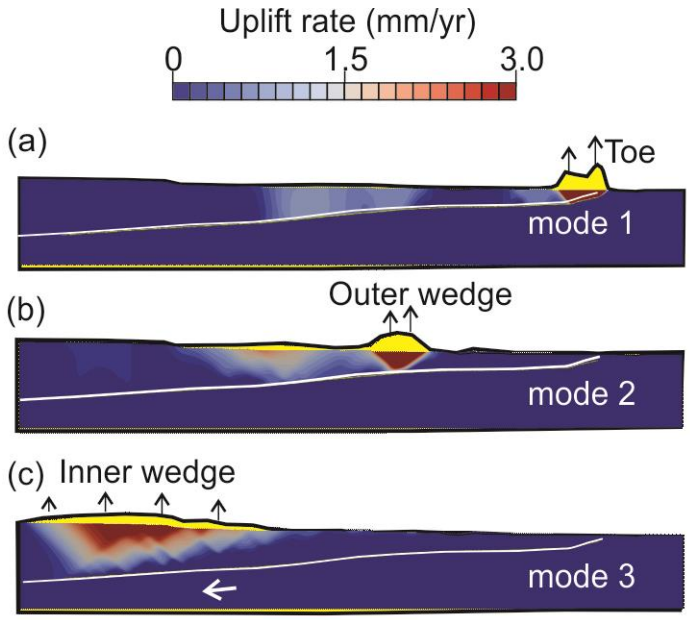

Figure 3. Illustration of the three main modes of wedge behaviour in model P1, with the model setup of Fig. 2b, but without faults. Results are shown after 5000 years of convergence. Colour shades show upward velocity (mm/yr), where red indicates zones of deformation where the wedge taper is growing (note that horizontal velocity component is not shown). The white curve highlights the location of the basal décollement. Arrows, and yellow region with black outline (vertical wedge displacement scaled up by (640×displacement/kyr) indicate the locus of vertical uplift. For all three panels, wedge friction coefficient μ_w = 0.8, décollement friction coefficient μ_b = 0.3, and faults are not included in the setup. (a) Mode 1 (stable sliding to toe) has wedge fluid pressure $\hat{\lambda}_w$ = 0.8 and high basal fluid overpressure (λ_b = 0.95). (b) Mode 2 (uplift of outer wedge, stable sliding inner wedge) is the same except λ_b = 0.88, and (c) mode 3 (uplift of inner wedge) has hydrostatic wedge and basal fluid pressure $\hat{\lambda}_w$ = 0.4 and λ_b = 0.4.

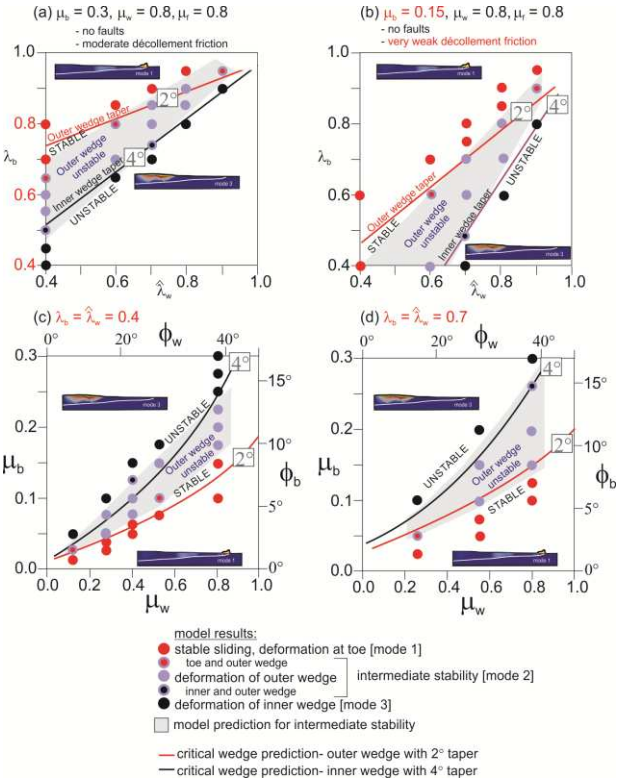

Figure 4. Stability analysis for model P1. Uniform wedge and décollement frictional properties are assumed throughout. Wedge material has a small cohesion of 1 MPa and décollement has a cohesion of 0.1 MPa (Table 1). The red and black lines plot the (λ_b, $\hat{\lambda}_w$) values for which critical wedge theory predicts stable sliding for a taper of 2° (red, outer wedge) and 4° (black, inner wedge). The coloured dots are model results, as described in the legend. Grey shading indicates intermediate (λ_b, $\hat{\lambda}_w$) values for which part of the wedge is stable but not the whole wedge, based on model results. (a) Model P1a- basal décollement friction 0.3, wedge friction 0.8, no fault weakening. The grey region deviates from cohesion-less critical wedge theory bounds at high fluid pressures owing to the prescribed cohesion of 1 MPa. Red labels on y-axis indicate the three (λ_b, $\hat{\lambda}_w$) values used in Fig. 3. (b) the same as (a) except that décollement friction coefficient is 0.15. (c) Model P1b- fluid pressure ratio held constant and hydrostatic everywhere (λ_b= $\hat{\lambda}_w$ = 0.4) while wedge and décollement friction coefficient are varied. Bottom and left axes are wedge and décollement average friction coefficients (μ_w and μ_b), respectively. Top and right-hand axes show equivalent angles of internal friction. (d) Same as (c) but for a fluid pressure ratio of 0.7 everywhere. In (b-d), red text at top of sub-figures highlights changed input parameter values cf. (a).

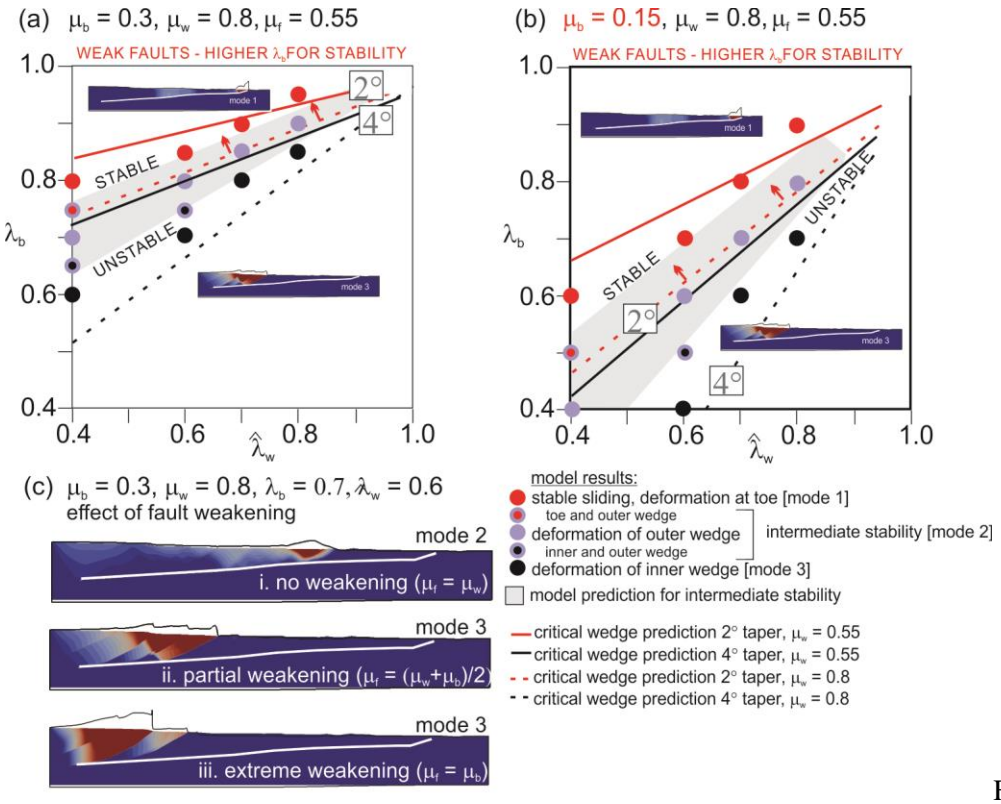

Figure 5. Stability analysis for model P2 where inclusion of the upper plate faults results in a weakened wedge. The dashed red and black lines plot the (λ_b, $\hat{\lambda}_w$) values for which cohesionless critical wedge theory (with no weak faults in the wedge) predicts stable sliding for a taper of 2° (red, outer wedge) and 4° (black, inner wedge). The solid red and black lines show predictions for critical wedge theory where the entire wedge has fault friction coefficient of 0.55. Grey shading indicates (λ_b, $\hat{\lambda}_w$) values with intermediate wedge stability, based on model results. (a) Basal décollement friction coefficient 0.3, wedge friction coefficient 0.8, fault friction coefficient 0.55, fault cohesion 0.1 MPa. The addition of weak faults shifts the grey zone towards higher values of λ_b relative to critical wedge predictions (as indicated by red arrows). (b) the same as (a) except that the décollement friction coefficient is reduced to 0.15. (c) An example showing the change in wedge mode as faults are progressively weakened, with an upward shift in the stability field (grey to pink shading, panel at right) causing a transition from mode 2 intermediate stability to mode 3 inner wedge deformation, as weak faults influence the overall strength in the wedge and return it to a subcritical state. Progressive weakening is illustrated by panels (i) no fault weakening; (ii) partial weakening with fault friction 0.55; (iii) extreme weakening with fault friction = décollement friction.

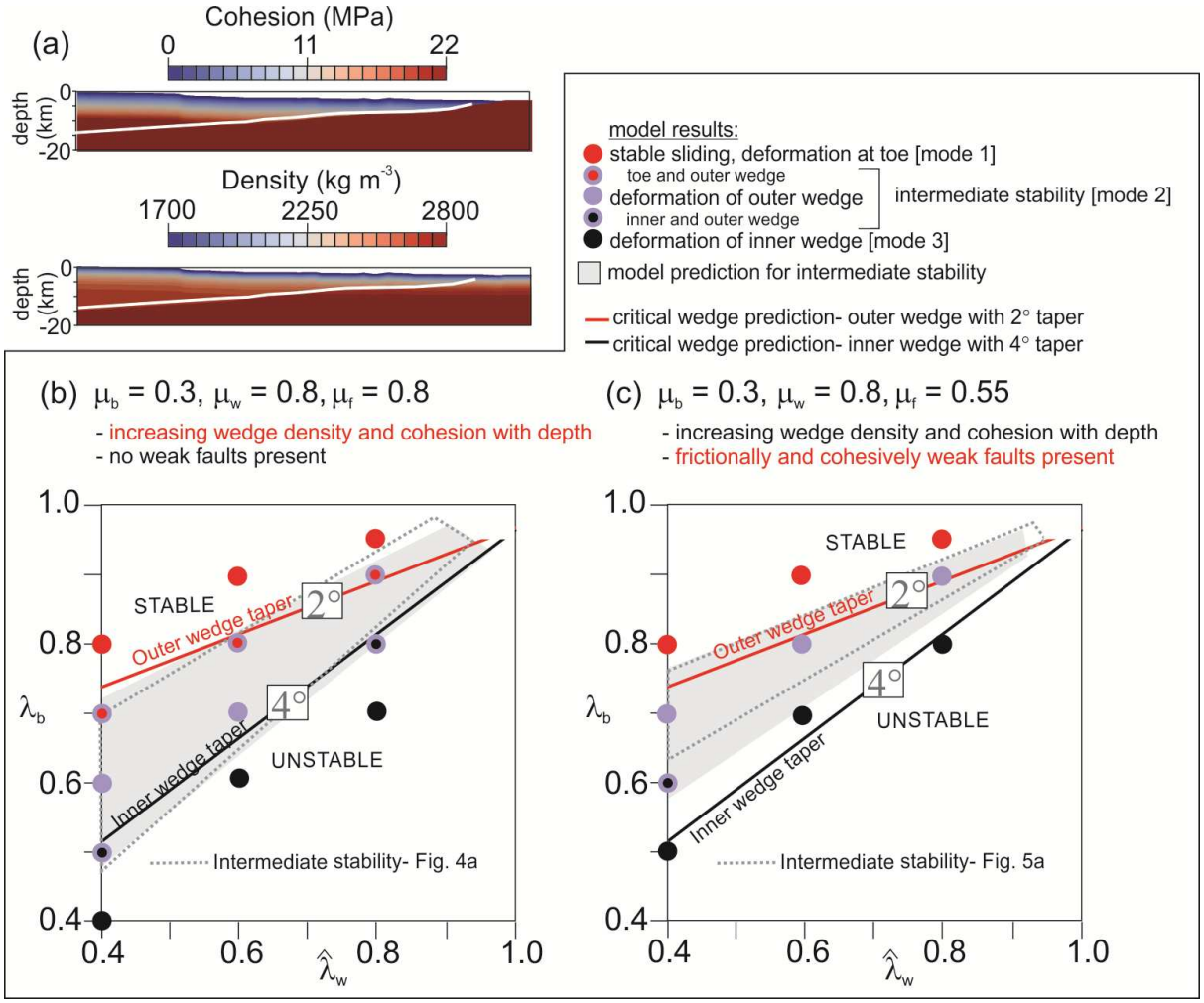

Figure 6. Stability analysis for model P3- investigating the role of increasing density and cohesion with depth and effective pressure. (a) Increase in cohesion and density with depth. Décollement shown in white. (b) Basal décollement friction coefficient 0.3, wedge friction coefficient 0.8, no faults. Décollement cohesion is 0.01 MPa, otherwise cohesion and density increase with depth as described in the text and shown in panel (c). The red and black lines plot the (λ_b, $\hat{\lambda}_w$) values for which cohesionless critical wedge theory predicts stable sliding for a taper of 2° (red, outer wedge) and 4° (black, inner wedge). Grey shading indicates (λ_b, $\hat{\lambda}_w$) values with intermediate wedge stability, based on model results. Grey dashed polygon indicates intermediate stability range from Fig. 4a (equivalent case with constant density and cohesion), for comparison. (c) Same as in (b) but with weak faults included. The weak faults have a low friction coefficient of 0.55, and a low cohesion of 0.1 MPa. Grey dashed polygon indicates intermediate stability range from Fig. 5a (equivalent case with constant density and cohesion), for comparison.

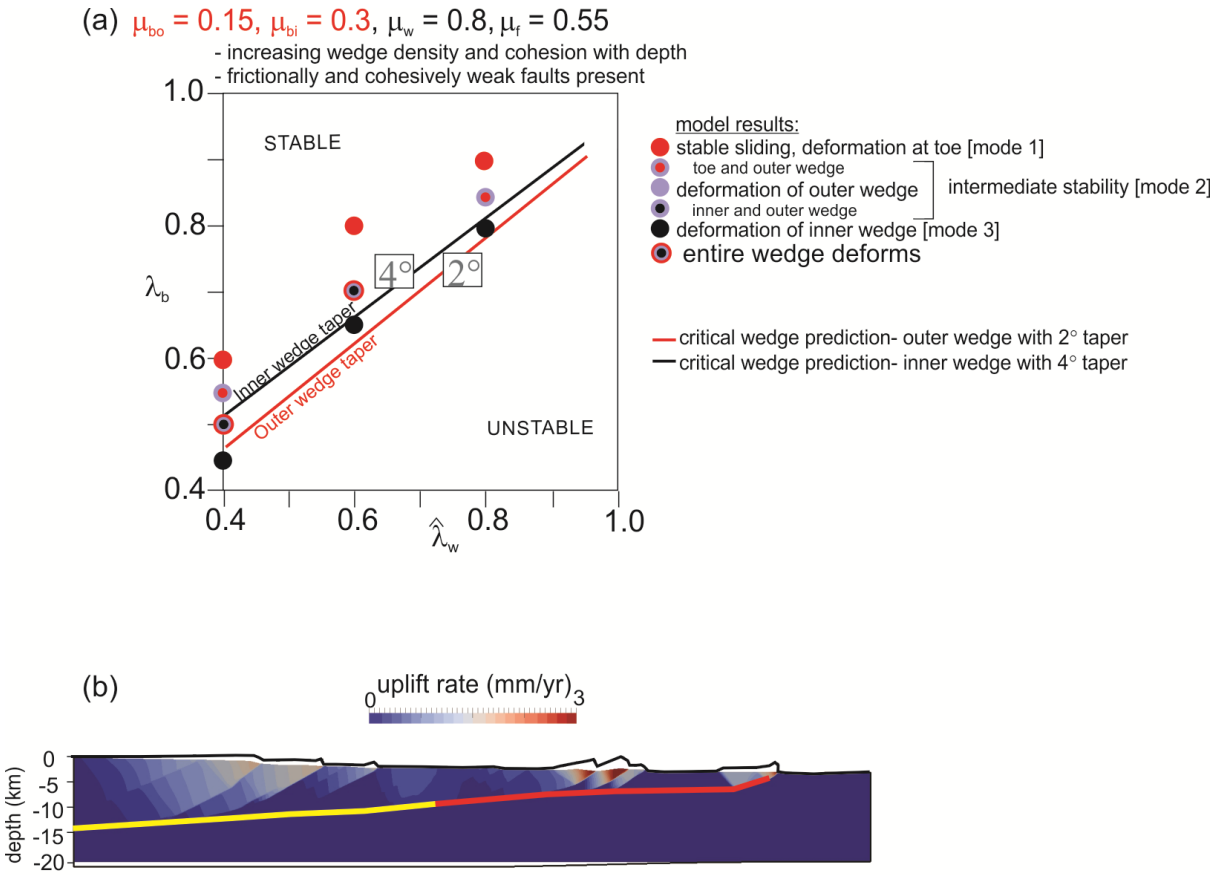

Figure 7. (a) Stability analysis for model P4, with weak faults and increasing density and cohesion with depth like model P3, but where the basal décollement friction coefficient is higher for the inner wedge than the outer wedge. Coloured circles show same modes as in previous models, but with an additional mode of wedge behaviour ("entire wedge deforms") as indicated. (b) shows this additional mode, with uplift at the back, middle, and toe of the wedge. The coloured bold lines show the location of the inner (yellow) and outer (red) basal décollements.

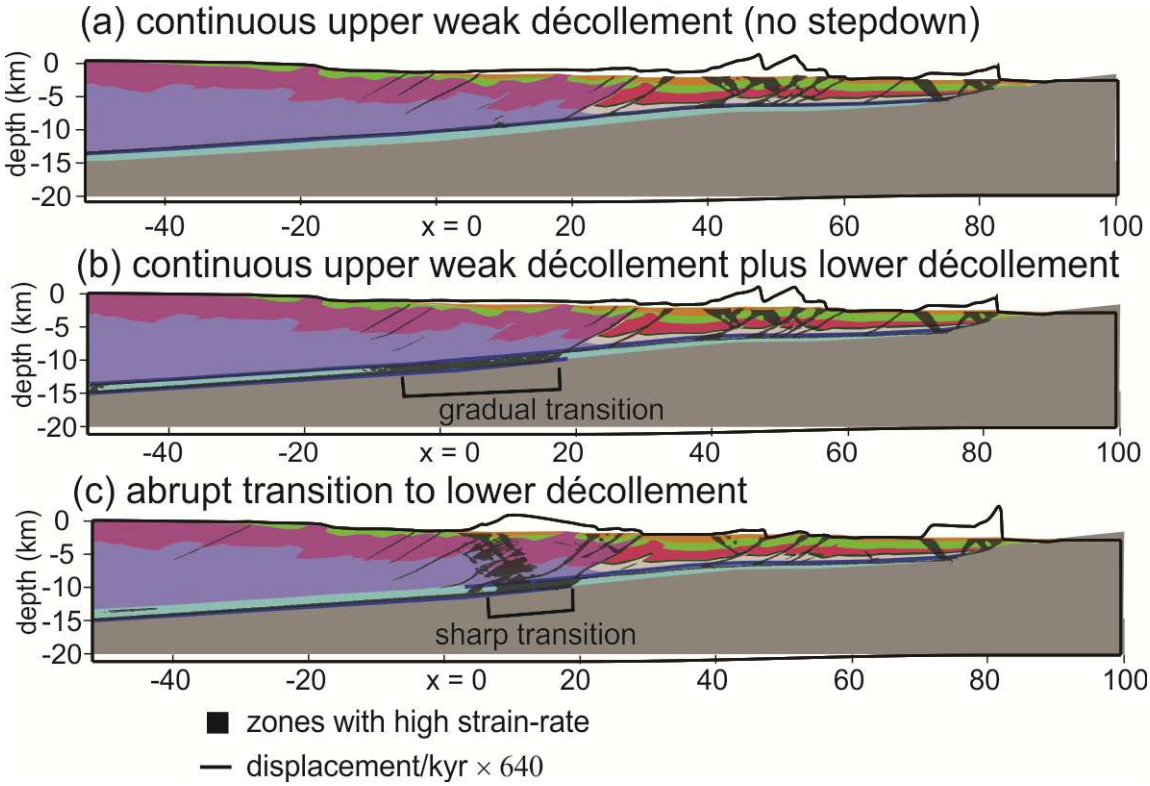

Figure 8. Model P5, with a lower décollement present beneath the inner wedge (dashed blue line on Fig. 2a). Each panel shows regions that have high strain-rates (second invariant $>5\times10^{-15}$ s^{-1}) superimposed onto ET2 wedge stratigraphy from Fig. 2a). Actively straining faults are shown in black. Other frictionally weak fault zones are present in the model (red lines in Fig. 2a) but are not shown in this figure. Black line above the surface shows vertically exaggerated displacement profiles (640×displacement/kyr). (a) Model with no décollement step-down. Friction and fluid ratios have bene selected to cause deformation of only the outer wedge and toe: wedge sediments have friction coefficient 0.8, fault friction coefficient 0.55, and hydrostatic wedge fluid pressure ratio $\hat{\lambda}_w = 0.4$. Décollement has friction coefficient 0.3 and fluid overpressure ratio $\lambda_b = 0.8$. (b) The same model, but with a second weak décollement layer (located at the base of subducting sediment beneath the inner wedge) that is given the same frictional properties and fluid pressure ratio as the upper décollement. A gradual step-down occurs over a ca. 20 km-wide zone, resulting in insignificant additional low-amplitude uplift of the Pōrangahau Ridge region. (c) A model where the upper weak layer is cut off beneath Pōrangahau Ridge, forcing the décollement to step down sharply and producing uplift rates comparable in magnitude to those at the toe of the wedge.

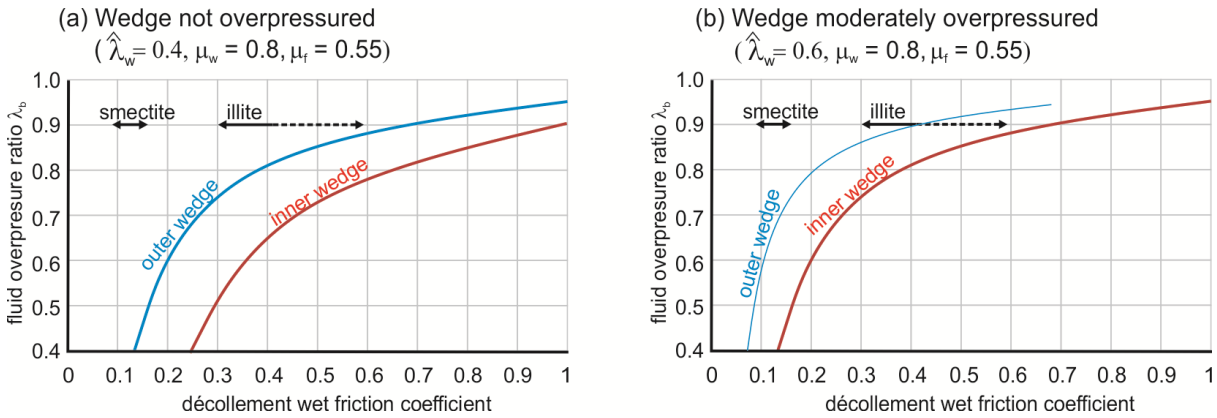

Figure 9. Curves indicating minimum décollement fluid pressure ratio required, vs. wet sediment décollement friction coefficient, as predicted by critical wedge theory for (a) hydrostatic fluid pressure in the wedge; and (b) moderate overpressure in the wedge. Blue curve is for the lower-tapered outer wedge and red curve is for the higher taper of the inner wedge. Based on Fig. 6b, we take required effective friction coefficient $(\mu_{bo})' \leq 0.08$ (a) and ≤ 0.04 (b); and $(\mu_{bi})' \leq 0.15$ (a) and ≤ 0.08 (b), respectively. For comparison, a range of stable sliding friction coefficients for saturated 100% montmorillonite and 100% illite are shown (black solid arrow, labelled; based on Morrow et al., 2017 (saturated montmorillonite), Saffer and Marone, 2003 (illite), Ikari et al. 2009a (illite), Behnsen and Faulkner, 2012 (illite and montmorillonite)). Dashed lines represent illite-quartz and montmorillonite-quartz mixture strengths in Tembe et al. (2010) and Ikari et al. (2009a). Note that decreasing amounts of clays within a gouge or mélange will result in increasing strength (e.g., Fagereng and Sibson, 2010; Tembe et al., 2010) unless the clays form a continuous foliation along which sliding occurs (e.g., Collettini et al., 2009) or the mixture slips coseismically (e.g. Faulkner et al., 2011).

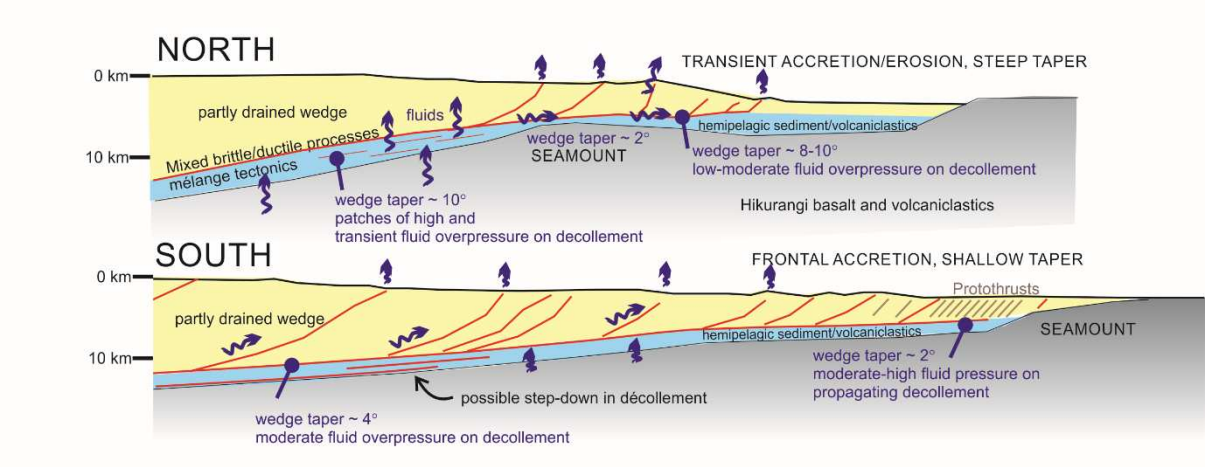

Figure 10. Schematic comparison between (a) northern Hikurangi (profile 05CM-04 offshore Gisborne; Barker et al., 2009, 2018; Bell et al., 2010; Ellis et al., 2010; 2015; Antriasian et al., 2019) and (b) south-central Hikurangi (profile ET2 discussed in this paper). Subducting sediment shown in light blue, subducting lower plate in grey, and wedge in yellow. Major thrust faults in red. Blue arrows indicate fluid pathways. More fluid sources and upward fluid connectivity from the subducting slab in the north vs. the south are speculatively indicated, based on fluid chemistry showing a greater slab-derived component in the north (Reyes et al., 2010) and inferences about slab dehydration state from plate reconstructions and tomography (Eberhart-Philips et al., 2017).

Table 1. Model parameters

Parameter	*Model P1a [P1b]*			*Model P2*	*Models P3-P5*
	Friction coefficient	Cohesion (MPa)	Bulk Density (kg m^{-3})		
Subducting plate	0.84	25	2800	Same as P1	Same as P1
Subducting sediment	0.8	1	2500	Same as P1	Same as P1 except cohesion, density derived from effective pressure
Décollement	μ_b= 0.15 or 0.30 [variable]	0.01	2500	Same as P1	Same as P1**
Wedge sediment	μ_w = 0.8 [variable]	1	2500	Same as P1	Same as P1 except cohesion, density derived from effective pressure
Upper plate Faults	$\mu_f = \mu_w$	1	2500	μ_f =0.55, cohesion = 0.1 MPa, density = 2500 kg m^{-3}	$\mu_f = \mu_w$ or 0.55; cohesion 0.1 MPa or derived from effective pressure, density derived from effective pressure
Basal fluid pressure ratio λ_b	0.4-0.95 [0.4 or 0.7]*			0.4-0.95	0.4-0.95
Average wedge fluid pressure ratio $\hat{\lambda}_w$	0.4-0.95 [0.4 or 0.7]*			0.4-0.95	0.4-0.95
Fault fluid pressure ratio λ_f	$=\hat{\lambda}_w$			$=\hat{\lambda}_w$	$=\hat{\lambda}_w$

*Note that in model P1b (Fig. 4c, d), friction coefficients are varied whilst fluid pressure ratios λ_b and $\hat{\lambda}_w$ are held constant at 0.4 or 0.7, as indicated in square brackets. **In model P5, there is an additional décollement at the interface between subducting sediment and the subducting plate, with the same properties.